universität wien

MASTERARBEIT / MASTER'S THESIS

Titel der Masterarbeit / Title of the Master's Thesis

Investigation of beam-induced dynamics in oxide glasses via aXPCS

verfasst von / submitted by

Michael Legenstein, BSc

angestrebter akademischer Grad / in partial fulfilment of the requirements for the degree of

Master of Science (MSc)

Wien, 2018 / Vienna, 2018

Studienkennzahl lt. Studienblatt / degree programme code as it appears on the student record sheet:	A 066 876
Studienrichtung lt. Studienblatt / degree programme as it appears on the student record sheet:	Masterstudium Physik
Betreut von / Supervisor:	ao. Univ.-Prof. Mag. Dr. Bogdan Sepiol

Abstract

Investigating diffusion in solid state matter has been a long-standing challenge. In recent years a new technique called atomic-scale X-ray Photon Correlation Spectroscopy (aXPCS) has emerged. Its working principle is the same as for the long established Dynamic Light scattering, but with X-rays instead of visible light. The successful realization of an aXPCS experiment was made possible by powerful new X-rays sources like third-generation synchrotrons and free-electron lasers.

Ideally, the X-ray beam would only measure internal dynamics and leave the system unperturbed otherwise. However, a recent study has shown that the dynamics in vitreous silica and germanium, measured via aXPCS is proportional to the flux of the beam, while the dynamics in metallic glasses and single-crystalline $Cu_{90}Au_{10}$ does not show this behaviour. This indicates that aXPCS does not only probe dynamics in some materials like oxide glasses, but also induces dynamics. Further investigations of this beam-induced dynamics will be the focus of this thesis.

The thesis begins with a theoretical treatment of aXPCS as well as network glasses in general and oxide glasses in particular. Then the experimental approach and the data evaluation process will be presented in detail.

In the main part the effects of the beam on the dynamics of a wide range of oxide glasses will be investigated. It will be shown that the dynamics in all glasses show a dependence on the photon flux. The dynamics measured at room temperature is proportional to the flux in all glasses, indicating that the dynamics is entirely beam-induced. At temperatures well above room temperature the influence of the beam becomes significantly smaller, hinting at a mixture of beam-induced and internal dynamics.

Furthermore, the characteristics of the induced dynamics will be explored in detail. Finally, the consequences of beam-induced dynamics on future aXPCS experiments will be discussed and some possible mechanisms underlying beam-induced dynamics presented.

Zusammenfassung

Das Erforschen von Diffusionsprozessen in Festkörpern ist seit jeher eine große Herausforderung. In den letzten Jahren ist mit der atomaren Röntgen-Photonen-Korrelationsspektroskopie (aXPCS) eine neue Technik aufgekommen die es ermöglicht Diffusionsprozesse auf atomarer Ebene zu beobachten. Das Prinzip hinter der Methode ist dasselbe wie bei der etablierten Methode der dynamischen Lichtstreuung, nur dass bei aXPCS Röntgenstrahlen verwendet werden anstelle von sichtbarem Licht. Die erfolgreiche Etablierung wurde möglich durch neue, leistungsstarke Quellen für Röntgenstrahlen wie Synchrotrons der dritten Generation und Freie-Elektronen-Laser.

Idealerweise dienen die Röntgenstrahlen zur Messung von internen Dynamiken und lassen das System sonst ungestört. Jedoch haben kürzlich durchgeführte aXPCS Messungen an gläsernem Silizium und Germanium gezeigt, dass die Dynamiken proportional zum Photonenfluss des Röntgenstrahls sind. Dieses Verhalten konnte in ebenfalls gemessenen metallischen Gläsern und dem Einkristall $Cu_{90}Au_{10}$ nicht beobachtet werden. Die Fluss-Abhängigkeit deutet darauf hin, dass aXPCS nicht nur interne Dynamiken in einigen Materialien wie Oxidgläsern misst, sondern auch selbst erzeugt. Diese induzierte Dynamiken sind der Hauptfokus dieser Arbeit.

Die Arbeit beginnt mit einer theoretischen Abhandlung von aXPCS, sowie Netzwerkgläser im Allgemeinen und Oxidgläser im Speziellen. Danach wird die experimentelle Vorgehensweise und die Datenauswertung im Detail behandelt.

Im Hauptteil dieser Arbeit werden die Auswirkungen des Röntgenstrahls auf die Dynamik in einer breiten Auswahl an Oxidgläsern untersucht. Es wird gezeigt, dass die Dynamik in allen Gläsern eine Abhängigkeit vom Photonenfluss aufweist. Die bei Raumtemperatur gemessene Dynamik ist bei allen Gläsern proportional zum Photonenfluss. Das ist ein starkes Indiz dafür, dass jegliche gemessene Dynamik strahlinduziert ist. Bei Temperaturen deutlich über der Raumtemperatur wird der Einfluss des Strahls merklich geringer, was auf eine Mischung aus interner und induzierter Dynamik hinweist.

Weiters werden die Eigenschaften der induzierten Dynamik genauer untersucht. Schlussendlich werden die Auswirkungen der strahlinduzierten Dynamik auf zukünftige aXPCS Experimente diskutiert und mögliche Mechanismen die diesen Dynamiken zugrunde liegen präsentiert.

Contents

Chapter 1

Introduction

There are a variety of methods to investigate diffusion in matter. A rough overview is given in Fig. 1.1. However, it is still extremely challenging to develop a feasible technique for studying the motion in hard solid matter on an atomic level. Two requirements must be fulfilled. Firstly, the spatial resolution must be in the order of Ångstrom. Secondly, the energy range of the technique must cover small frequencies since atomic motion in solid matters is relatively slow. A recently developed method that fulfils both requirements is called atomic-scale X-ray Photon Correlation Spectroscopy (aXPCS)[1]. It was developed from the long-existing Photon Correlation Spectroscopy (PCS) or Dynamic Light Scattering[2](DLS) respectively. DLS uses visible light, while aXPCS uses hard X-Rays[1] to probe matter. Like its predecessor, aXPCS studies the temporal change in speckle patterns projected at the detector by the scattered radiation. To make the technique feasible, a coherent X-ray source with a high flux of photons is necessary.

The successful implementation of aXPCS was made possible by modern third-generation synchrotrons and free-electron lasers. They are able to produce X-Rays in a wide energy range and with a high degree of coherence. They also have an unrivalled brilliance[2] compared to any other source of X-rays. The high brilliance comes with a price though. There is always an unavoidable interaction between beam and sample and the higher the photon flux[3] is, the higher the chance that the beam will have a distorting effect on the experiment. There are two possible consequences of the interaction with the sample. It can have either permanent effects, i.e. radiation damage, or temporal effects on the sample and therefore changes the outcome of the experiment. When conducting an experiment it is crucial to know what this effects are and how the influence the results to interpret them correctly. The consequences of this unavoidable interaction between beam and the sample depend both on the energy and flux of the beam and the sample material that is probed.

Radiation damage, that is a permanent change in the atomic structure, is a well known artefact in soft matter physics. Soft matter is matter that is easily deformed by mechanically or thermal stress, like polymers and biological samples. The effects on X-rays on this materials range from small chemical rearrangements to the complete destruction of the sample[3]. This effects have been studied intensively in the past and are well known today.

For hard matter the situation is quite different. A silent consensus that hard X-rays do not damage samples made of hard matter permanently has existed in the past. However, there is no

[1] X-rays with photon energies above 5 to 10 keV are commonly called hard X-rays, those with lower energy are called soft X-rays.

[2] Brilliance $= \frac{\text{number of photons}}{\text{second}\cdot\text{mrad}^2\cdot\text{mm}^2\cdot 0.1\%\text{Bandwidth}}$

[3] Flux $= \frac{\text{number of photons}}{\text{second}\cdot\text{mm}^2}$

good reason to assume that dynamics is also not influenced by a high intensity beam of hard X-rays. There have been few studies on this subject. The first experiment investigating possible beam-induced dynamics was conducted bei Leitner et al[4]. They performed an aXPCS experiment with a single-crystalline $Cu_{90}Au_{10}$ at the beamline P10, PETRA III in Hamburg. In this experiment, the energy of the beam and temperature of the sample were fixed. To test the beam's effect on the sample they varied its intensity by inserting different numbers of attenuators. What they found was that the dynamics did not depend on the intensity of the beam. This indicates that there are either no beam-induced effects on the material investigated or that the dynamics was too fast to detect with their experimental setup.

In 2016 a group at the beamline ID10, ESRF in Grenoble performed a conceptually similar experiment. Instead of single-crystalline $Cu_{90}Au_{10}$, they used vitreous silica Si_2O, vitreous germania Ge_2O and a metallic glass with the composition $Cu_{65}Zr_{27.5}Al_{7.5}$. The first two materials are simple oxide glasses. To everyone's surprise they found that the X-rays generate a non-trivial stationary dynamics[5] in this two oxide glasses and the dynamics was dependent on the number of attenuators inserted. The metallic glass on the other hand did not show any flux dependence at all. Hence, the measurements of the oxide glasses stand in contrast to the work of Leitner et al. and are hinting to the presence of beam-induced dynamics, while the metallic glass confirms them.

This results indicate that different types of hard matter are influenced in a different way by hard X-rays, some of them showing beam-induced dynamics and some are not.

In the course of this thesis further aXPCS experiments on oxide glasses were conducted to study this stationary dynamics caused by the beam. The main goal of this thesis is to gain detailed insides on how the photon flux influences the dynamics for different glass compositions and temperatures. Additionally, an attempt to give a theoretical explanation of the interaction between matter and hard X-rays will be made.

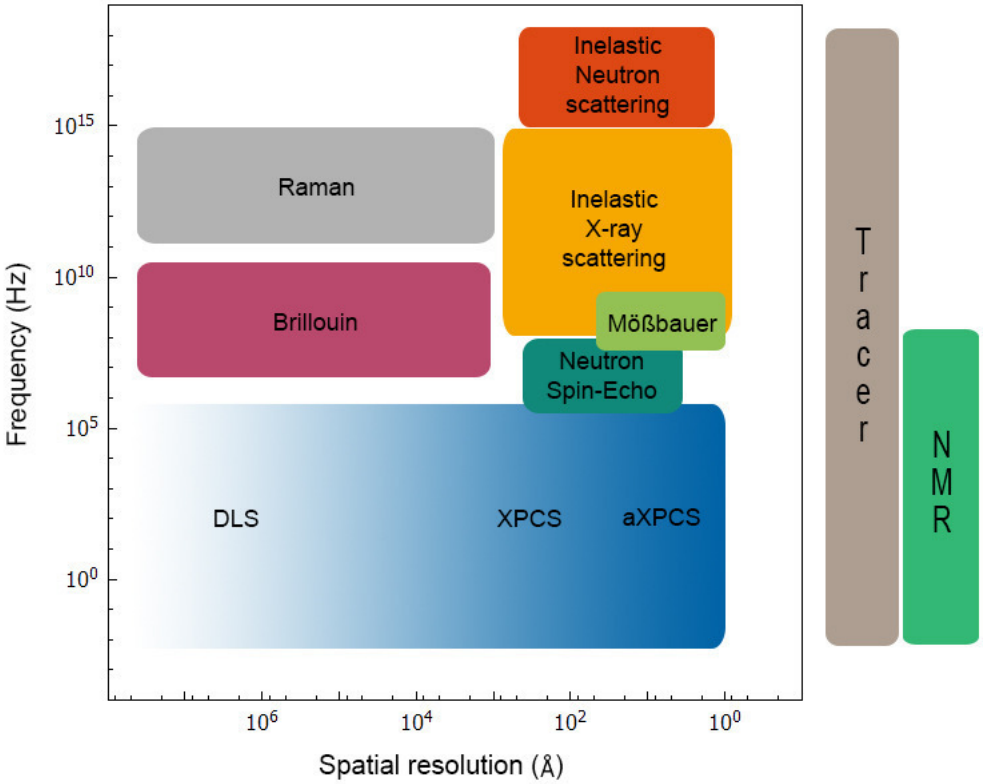

Figure 1.1: Overview of available methods to measure diffusion in hard matter. The axis show the typical lengths (x-axis) and frequencies (y-axis) of the dynamic structure factor $S(Q \propto length^{-1}, \omega)$ that can be accessed by the respective method. Tracer diffusion measurements and nuclear magnetic resonance spectroscopy (NMR) are only plotted with respect to the frequency, since they are macroscopic methods and therefore are not able to resolve microscopic dynamics.

Chapter 2

aXPCS: Studying diffusion on the atomic scale

aXPCS is a fairly new technique, although the idea behind it is not so new. As mentioned in the introduction, it is already an established technique with visible light called *Dynamical light scattering* [2] (DLS). aXPCS can be classified as an elastic scattering technique, working in the time domain and based on hard X-rays with a need of a high photon flux and a high degree of coherence.

X-rays have a wavelength ranging from 0.01 to 10 nm. This is the same order of magnitude as typical distances of atoms in solid state matter. This makes X-rays the perfect tool for diffraction experiments on the atomic scale.

Atomic diffusion in glasses is in general relatively slow at temperatures where the glass is solid and an amorphous (i.e. not recrystallizing) material. The scattering vector is in the Ångstrom regime which makes aXPCS, at the time this thesis was written, the only technique to investigate it.

2.1 Working principle

It is known from diffraction theory, that a beam of X-rays hitting a disordered system, e.g. glass, the radiation scatters in all directions and angles with respect to the incoming beam. In general, the scattered intensity is a function of scattering angle and direction, i.e. $I = I(\mathbf{q})$. In contrast to ordered systems, the scattered intensity $I(\mathbf{q})$ in glasses is equally distributed in all directions. Due to this symmetry, the intensity $I(\mathbf{q})$ only depends on the absolute value of $\mathbf{q}$, i.e. $I = I(q)$. The exact form of $I(q)$ depends on the structural composition of the glass.

The intensity $I(q)$ seen at the detector for some chosen value of q is a pattern of seemingly randomly positioned speckles with dark spots in between. The ratio between dark spots and the speckles will of course depend on the flux of the incoming beam and on the scattering power for the chosen q-value. It turns out however that the positions of the speckles are not random after all. They depend on the position of the atoms in the disordered system. The diffracted photons can either interfere constructively (light regions, i.e. speckles) or interfere destructively (dark regions) during the scattering, resulting in the before mentioned speckle pattern. If there is ongoing diffusion in the material, the positions of some atoms are changing over time. With the position of the atoms changing, the areas that interfere constructively and destructively also change. This leads to a change of the speckle pattern over time. This temporal change of the speckles is recorded by the detector and then used to measure and gain information about dynamics in the material investigated

(see Fig. 2.1).

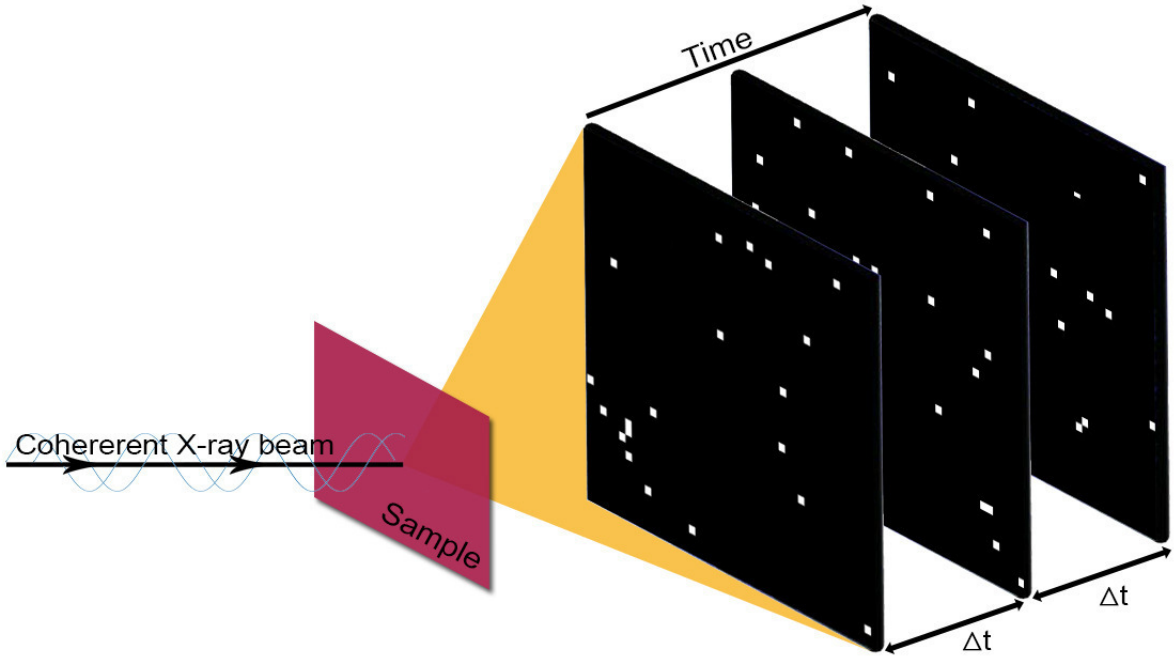

Figure 2.1: A sample gets irradiated with a coherent high-intense X-ray beam. An area detector is placed at an angle 2θ. Due to interference the X-ray beam produces a speckle pattern at the detector. A time series of speckle patterns is measured. Atomic motion in the sample causes the speckle pattern to change over time, from which information of the diffusion process can be gained by calculating the autocorrelation function of the intensity at the detector.

2.2 Light sources for aXPCS

For dynamic light scattering, laser light provides an optimal light source, since it is coherent and has a high intensity. The situation for X-rays is more difficult since there have not been suitable sources in the past. This has changed with the upcoming of third-generation synchrotrons and free-electron lasers. Both provide X-rays with coherence and intensity high enough for coherent scattering. This led to the implementation of atomic X-Ray photon correlation spectroscopy. aXPCS is capable of measuring low frequency dynamics (10^6 Hz to 10^{-3} Hz) in a q-range from typically $1 \cdot 10^{-3}$ Å^{-1} to several Å^{-1} [6].

2.3 Coherent X-Ray scattering

The aforementioned speckles are caused by interference of all photons scattered by the atoms in the material. However, the speckles would change even without diffusion, if there was no fixed phase relation between the scattered photons. Hence a high degree of coherence is crucial for a successful aXPCS experiment. Otherwise only noise would be detected.

It will be shown later that the Signal-to-Noise Ratio (SNR) is approximately proportional to the degree of coherence. The issue of coherence can be split up in two parts. Firstly, the coherence

of the incoming beam needs to be characterized. Secondly, the coherence loss of the scattered radiation, caused by the difference in path length during scattering, must be discussed.

2.3.1 Coherence of the incoming beam

Light sources can be classified into sources that are based on stimulated emission, i.e. laser light, and chaotic light sources. A laser is an ideal coherent light source, since the process of stimulated emission guarantees a well-defined phase relation between all the photons in the beam. Unfortunately, this does not hold for chaotic light sources based on spontaneous emission. Chaotic sources are, for example, light bulbs, X-Ray tubes and also synchrotron radiation facilities. For this source types the coherence can be characterized in terms of the longitudinal coherence length ξ_l and the two transversal (vertical, horizontal) coherence lengths $\xi_{v,h}$ [7]. The longitudinal coherence length ξ_l is given by

$$\xi_l \approx \frac{\lambda}{2(\Delta\lambda/\lambda)}, \tag{2.1}$$

while the transversal coherence length $\xi_{v,h}$ is given by

$$\xi_{v,h} \approx \frac{\lambda L}{2D_{h,v}}. \tag{2.2}$$

Here, λ is the wavelength of the beam, $\Delta\lambda$ is the spreading of the wavelength at full width of half maximum, L the distance from source to sample and $D_{v,h}$ is the source size in vertical and horizontal direction. The coherent volume is spanned by the transverse and longitudinal coherence lengths, giving the coherence volume

$$V_{\mathsf{coh}} = \xi_v \cdot \xi_h \cdot \xi_t \approx \frac{\lambda^2 \cdot L}{4(\Delta\lambda/\lambda)D_{h,v}}. \tag{2.3}$$

However, in an actual experiment the illuminated volume is usually smaller than the coherent volume, leading to a loss of coherence. The degree of coherence β can be estimated by the formula [8]

$$\beta \approx \frac{V'_{\mathsf{coh}}}{V_{\mathsf{ill}}}. \tag{2.4}$$

V_{ill} is the illuminated volume, while V'_{coh} is the volume that is spanned by either the coherence length or the beam width in the respective dimension, depending on which is smaller. In the common case, i.e. the traversal coherence $\xi_{\mathsf{v,h}}$ is larger than the beam width W the formula reduces to

$$\beta \approx \frac{\xi_l}{W}. \tag{2.5}$$

2.3.2 Coherence loss within the sample

Unfortunately, coherence is lost to some degree while the beam travels trough the sample. The maximum path length difference (PLD) is defined as the difference between the shortest and the longest geometrical path that a photon takes through the sample. A setup for a typical X-ray diffraction experiment in transmission geometry is shown in Fig. 2.2. The beam has a diameter d, the sample thickness is W and the diffraction angle is 2θ. For this geometry, the maximal PLD for a photon is

$$P = p_1 + p_2 - p_3. \tag{2.6}$$

After some rearrangements of Eq. (2.6), the maximum PLD can be expressed as a function of d, W and θ:

$$P = d \cdot \sin(2\theta) + 2W \cdot \sin^2(\theta) \tag{2.7}$$

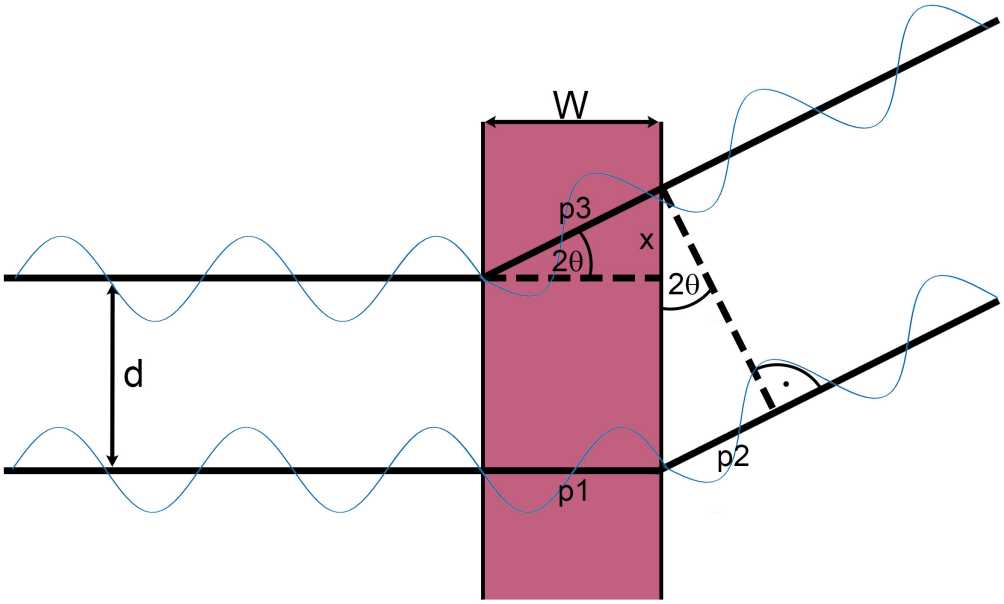

Figure 2.2: The path length difference for two photons that are at a maximal distance d. Due to this difference the phase relation between the photons changes. This causes a loss in coherence.

To not loose coherence due to differences in the path length, the maximum PLD must be smaller than the longitudinal coherence length[7]:

$$P = d \cdot \sin(2\theta) + 2W \cdot \sin^2(\theta) \leq \xi_l \tag{2.8}$$

This condition was derived for maximal PLD. However, the PLD of most scattered photons will be less than this. Therefore, even if the condition is slightly violated, an aXPCS experiment is still possible, although with reduced contrast.

2.4 From speckles to diffusion dynamics

Physically, the speckle pattern is caused by the scattered intensity. The intensity is a coherent superposition of scattering probability amplitudes. Mathematically, this is expressed by the equation

$$I(\mathbf{q}, t) = \left| \sum_n f_n(\mathbf{q}) \exp(i\mathbf{q} \cdot \mathbf{r}_n(t)) \right|^2. \tag{2.9}$$

Here, $\mathbf{q}$ is the scattering vector, $f_n(\mathbf{q})$ is the scattering amplitude of the nth scatterer at position r_n and time t. The sum is taken over all scatterers, that are in the coherent volume. The exact

locations of the speckles are determined by the atomic configuration and the change of the speckles is caused by diffusion in the material. This raises the question, how this change of the speckle pattern can be measured. The mathematical tool to measure change in the electric field is the normalized, first-order time autocorrelation function (ACF). It is defined as

$$g^{(1)}(\mathbf{q}, \Delta t) = \frac{\langle E^*(\mathbf{q}, t) \cdot E(\mathbf{q}, t + \Delta t)\rangle_T}{\langle \left|E(\mathbf{q}, t)\right|^2 \rangle_T}, \tag{2.10}$$

The * denotes the complex conjugate of the electric field. The brackets $\langle\ \rangle_T$ indicate, that the time average has to be taken over the acquisition time T. From an experimental standpoint, Eq. (2.10) works for an experiment where a point detector is used. In the case an area detector is used, i.e. multi-speckle aXPCS, there has to be taken the average over all pixels additionally to the time average. This will be discussed in section 2.5.

A model for describing diffusion on the atomic level in solid state matter, that has been proven to work very well, is the jump diffusion model: Its basic assumption is that atoms stay most of the time at their position in the network of atoms, only vibrating around their equilibrium position. Diffusion occurs in the form of very fast jumps, contrary to the conception of continuous diffusion[1]. One jump diffusion model is the Chudley-Elliot model[9]. Chudley and Elliot were able to derive an analytical form for the first-order autocorrelation function:

$$g^{(1)}(\mathbf{q}, \Delta t) = e^{-\Gamma(\mathbf{q})\Delta t} \tag{2.11}$$

Here, $\Gamma(\mathbf{q})$ is called the decay parameter. $\Gamma(\mathbf{q})$ can be given in an analytical form for the Chudley-Elliot model. This model will be discussed in detail in section 3.4. The inverse of $\Gamma(\mathbf{q})$, $\tau = \Gamma^{-1}$, is called the characteristic decay time and connected to the diffusion constant D. In the limit $\mathbf{q} \to 0$, the decay parameter Γ, respectively the decay time τ, and the diffusion constant D are connected by[8]

$$\Gamma(\mathbf{q}) = \tau^{-1}(\mathbf{q}) = D \cdot q^2. \tag{2.12}$$

Eq. (2.11) is useful from a theoretical standpoint. Although the electric field cannot be measured directly and therefore, the first-order autocorrelation function cannot be measured. What can be measured are intensities of the electric field. For the correlation of the intensities, there is the second-order autocorrelation function. This function is given by

$$\begin{aligned} g^{(2)}(\mathbf{q}, \Delta t) &= \frac{\langle I(\mathbf{q}, t) \cdot I(\mathbf{q}, t + \Delta t)\rangle_T}{\langle I(\mathbf{q}, t)\rangle_T^2} \\ &= \frac{\langle E^*(\mathbf{q}, t)E(\mathbf{q}, t) \cdot E^*(\mathbf{q}, t + \Delta t)E(\mathbf{q}, t + \Delta t)\rangle_T}{\langle \left|E(\mathbf{q}, t)\right|^2 \rangle_T}. \end{aligned} \tag{2.13}$$

Furthermore, the first and second order ACFs are connected by the Siegert relation[10]:

$$g^{(2)}(\mathbf{q}, \Delta t) = 1 + |g^{(1)}(\mathbf{q}, \Delta t)|^2 \tag{2.14}$$

[1] Continuous diffusion is a suitable assumption for solids and gases, where particles are relatively free to move. It fails to work in solid state matter, where atoms are strongly bound within potential energy walls.

It must be pointed out that this equation is valid for a measurement with full coherence, i.e. the coherence factor $\beta = 1$. In the case of reduced coherence, i.e. $0 \leq \beta < 1$, the Siegert relation takes the form

$$g^{(2)}(\mathbf{q}, \Delta t) = 1 + \beta |g^{(1)}(\mathbf{q}, \Delta t)|^2. \tag{2.15}$$

With this relation, a functional form of the second-order autocorrelation function can be given:

$$g^{(2)}(\mathbf{q}, \Delta t) = 1 + \beta e^{-2\Gamma(\mathbf{q})\Delta t} \tag{2.16}$$

2.5 Multi-speckle aXPCS

In the previous section, all considerations were made under the assumption, that the experiment is done with a point detector. This can especially be seen in Eq. (2.10), where the averaging is only with respect to the time T. There is no averaging over an ensemble of pixels. However, averaging over a multitude of different pixels, can bring a tremendous increase in coherence, as will be shown here.

Firstly, to get from single-speckle to multi-speckle aXPCS, Eq. (2.13) must be modified:

$$g^{(2)}(\mathbf{q}, \Delta t) = \frac{\langle \langle I_p(\mathbf{q}, t) \cdot I_p(\mathbf{q}, t + \Delta t) \rangle_T \rangle_p}{\langle \langle I_p(\mathbf{q}, t) \rangle_T^2 \rangle_p} \tag{2.17}$$

This modified version takes the intensity $I_\mathrm{p}(\mathbf{q}, \Delta t)$ at pixel p, averages over all pixels and then takes the time-average over all frames. Furthermore, it must be kept in mind, that $\mathbf{q}$ is now a function of p, since it slightly varies for every pixel due to the finite size of any area detector. This can be neglected however, if the shift $\Delta\mathbf{q}$ is small compared to $\mathbf{q}$.

It has been shown that the signal-to-noise ration (SNR) for multi-speckle aXPCS is given by[11]

$$\mathrm{SNR} = \langle I \rangle \sqrt{N} \sqrt{m_b} \frac{\beta}{\sqrt{1 + \beta}}. \tag{2.18}$$

Here, $\langle I \rangle$ is the mean number of photons per pixel and per frame. N is the number of pixels, each with a size of a x a. m_b is the number of time bins, i.e. frames, for a measurement. Finally, β is the already known optical contrast. Eq. (2.18) shows that the SNR scales, amongst other factors, with the square root of the number of pixels.

For example, the detector at PETRA III, an Eiger 4M, had approximately 4 Million pixel, giving a contrast 2000 times higher than a point detector would have. In comparison to that, the detector at ESRF, an Andor CCD camera, had approximately 1 million pixel. This resulted in a factor of 2 in the difference of contrast between this detectors.

This numbers indicate that measurements with a point detector would have had a contrast so low, that no useful data would have been gained. Hence, for any aXPCS experiment, an area detector must be used.

2.6 Stretched exponential modification

Eq. (2.16) was derived under the assumption, that a single process is active and causing the diffusion. In a more general case, several processes can be active and causing diffusion at different rates. Then Eq. (2.16) must be replaced by the sum of multiple exponentials, each being accountable for

one diffusion process. This can be done in an approximative way by introducing the Kohlrausch-exponent[12] α, giving the modified version of the second-order ACF, the so called Kohlrausch-Williams-Watts (KWW) function[13]:

$$g^{(2)}(\mathbf{q}, \Delta t) = 1 + \beta e^{-2(\Gamma(\mathbf{q})\Delta t)^{\alpha}} \tag{2.19}$$

α can be a number between 0 and ∞. There are three cases that must be distinguished[8]:

- $\alpha > 1$:
  In this case the function is called a **compressed exponential function**. This is an indicator that the sample is not in an equilibrium state[2]. This can happen for example, when a glass sample is heated up and measured directly after the heating process. Then there is a possibility that the atoms are still in a process of rearrangement, which would result in an $\alpha > 1$.

- $\alpha = 1$:
  Here, the material is in an equilibrium state and there is just one diffusion process active.

- $0 < \alpha < 1$:
  In this case the function is called a **stretched exponential function**. The physical meaning of this is that there are several processes active, causing dynamics in the material.

2.7 Two-times correlation function

An additional mathematical tool for interpreting the results of an aXPCS measurement is the two-times correlation function. It is defined as the covariance of the scattered intensity[7],

$$C(\mathbf{q}, t_1, t_2) = \langle D(\mathbf{q}, t_1) \cdot D(\mathbf{q}, t_2) \rangle. \tag{2.20}$$

D(**q**,t) is the normalized intensity fluctuation. It is defined as

$$D(\mathbf{q}, t) = \frac{I(\mathbf{q}, t) - \langle I(\mathbf{q}, t) \rangle}{\langle I(\mathbf{q}, t) \rangle}, \tag{2.21}$$

where $\langle I(\mathbf{q}, t) \rangle$ is the average intensity, with the average being taken over all pixels for a given time t. The two-times correlation function is very useful to see whether a sample is in an equilibrium state or undergoing a structural transition, e.g. a phase transition or large-scale structural rearrangements, during the measurement.

An example to illustrate how the two-times correlation function works is shown in Fig. 2.3. As the name *two-times correlation function* already suggests, on both axes the time is plotted. This means, that the diagonal indicated by the black arrow is the line of same time, i.e. $t_1 = t_2$. Along this line the correlation is maximal for a given time $t = \frac{t_1+t_2}{2}$. Perpendicular to this line of equal time, the time difference Δt increases. Hence, along this path the correlation decreases, assuming that there is diffusion occurring. In the plot this is indicated by color, ranging from white (maximal correlation) over yellow, then red and finally to black (no correlation). The time difference until the

[2]The term *equilibrium state* has to be used carefully when talking about glasses, since they are never really in an equilibrium. However, non-equilibrium in this context means that there are large-scale structural rearrangements occurring. This is different from the frozen non-equilibrium (also called a meta-stable equilibrium) state glasses are normally in.

correlation falls by a factor of e^2, is indicated by dashed black lines. For the sample on the left the line has the same length for every time t of the measurement. This shows that the sample is in an equilibrium and not changing its structure over time. The sample on the right shows a broadening of the dashed line when the time moves forward, indicating a slowing of the dynamics in the sample. This is a clear indicator that the sample is not in an equilibrium. The reason for this is that the glass was heated up to 200 °C just before measurement. This lead to fast dynamics at the beginning that slowed down over time.

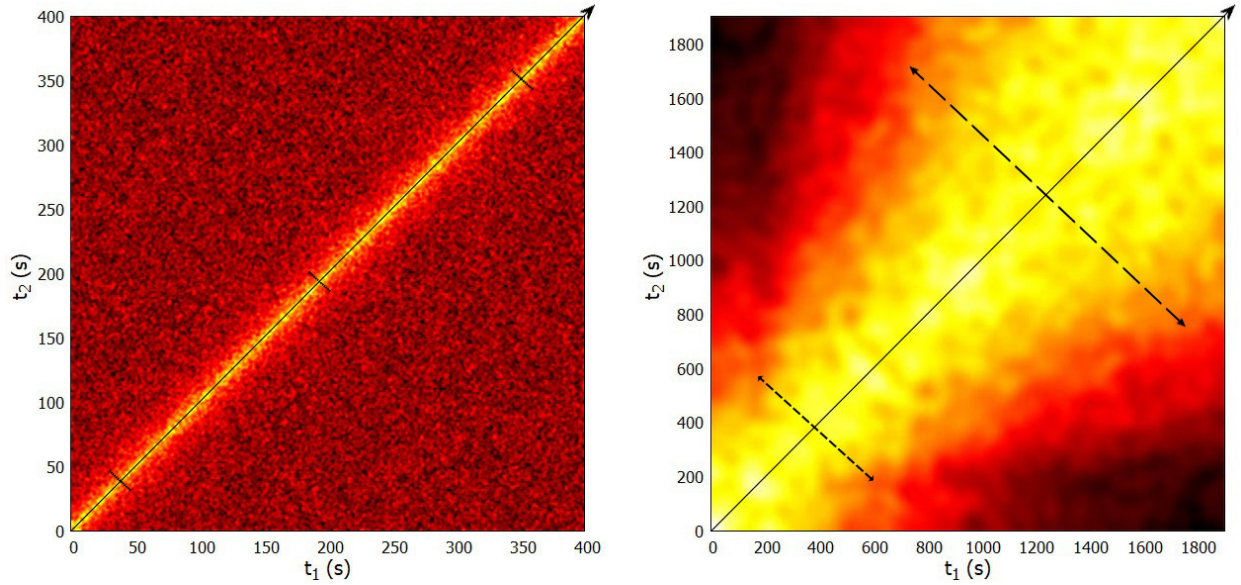

Figure 2.3: **Left:** $(V_2O_5)_{50}(P_2O_5)_{50}$ sample, T = 24 °C, 2θ=10°; **Right:** $(PbO)_{30}(SiO_2)_{70}$ sample, T = 200 °C, 2θ=10°

Chapter 3

Glasses: Structure and dynamics

The term *glass* refers to a wide range of different amorphous materials. All glasses have in common that they lack a long-range periodicity and symmetry in their atomic structure. This distinguish them from crystalline materials. The most common and historically the first type of glass are network glasses. The *Network formers* are the obligatory component in any network class. According to the widely accepted *Random Network Theory*, introduced by Zachariasen[14], they build up microscopical structures which are connected to each other building a three-dimensional random network. However, in terms of mole fraction, the network formers don't necessarily have to be the main component.

Three different network former will be introduced in this thesis. These are SiO_2, P_2O_5 and B_2O_3.

Beside the network formers a glass also can comprise *Network modifiers* and *Network intermediates*. Network modifiers are compounds which are not able to form networks on their own. By adding them, however, it is possible to change certain properties of the glass. This properties can be for example the electrical conductivity, the glass transition temperature or the color of the glass. A typical network modifier would be any alkali metal. Added to, for example a silicate glass, it lowers the melting point significantly (see Tab. 4.1) and also increases electric conductivity[15]. The network intermediates can act as both, network formers and modifiers.

3.1 Nomenclature

A nomenclature for describing different glass compositions is needed. Here, the stoichiometric style $(A_1)_{x_1}...(A_n)_{x_n}$ will be used. This means that the glass consists of n components A_i. Component A_i has a mole fraction of x_i (or mole% if multiplied by 100) with the condition that $\sum_i x_i = 1$. In general, a component is a molecule, not just a single element. For example, borate glass has the main component, i.e. the network former, B_2O_3. A typical network modifier would be lithium oxide Li_2O.

3.2 Oxide glasses

An important subtype of network glasses are oxide glasses. The network former in oxide glass has the formula (B_nO_m) for some element B with n atoms and oxygen with m atoms. B, n and m however can not be completely arbitrary. According to Zachariasen's theory there are selection rules when such a composition can form a random network instead of crystallizing. Additionally, one or

several network modifier $(A_1)_{x_1}...(A_n)_{x_{n-1}}$ can be added. The oxide glasses used in the course of this thesis, are silicate, borate and phosphate glasses.

3.2.1 Silicate glasses

Silicate glass has the chemical formula SiO_2. On a microscopical level they form SiO_4 tetrahedra that are connected to each other under different angles[16] forming a random network. The microscopical structure, called the short range order (SRO) unit, is shown in Fig. 3.1.

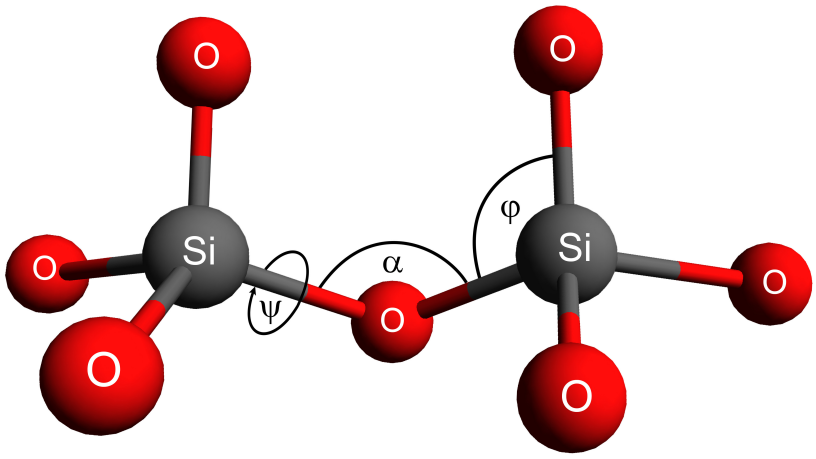

Figure 3.1: SiO_4 tetrahedra make up the basic building blocks of silicate glasses. The angle φ of the O-Si-O bond is fixed at a value of 109°28'. This specific angle is characteristic for tetrahedra in general. The tetrahedra are connected over the Si-O-Si bond with an angle α varying between 130° and 160°. The dihedral angle ψ is equally distributed between 0° and 180°.

As shown in Fig. 3.1, an oxygen atom that connects two polyhedra is called a bridging oxygen. The opposite is called a non-bridging atom. The nomenclature used for tetrahedral structures with bridging and non-bridging atoms is Q^i with i being the number of bridging oxygen. In the case of pure silicate glass, there are always four bridging oxygen for every tetrahedra, i.e. the structural unit is Q^4.

Studies by magic angle spinning NMR have shown that by adding alkali oxides, i.e. A_2O with a A being an alkali atom, the number of structural units changes[17]. The number of Q^4 units decreases, while all other units up to Q^3 increase. The situation is shown in Fig. 3.2.

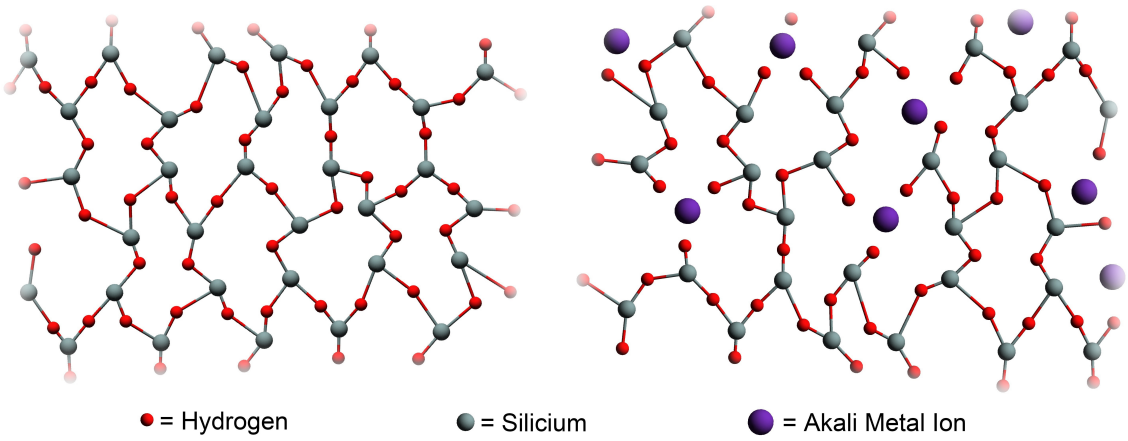

Figure 3.2: **Left:** Two-dimensional model of the structure of pure silicate glass. All oxygen atoms are bridging. **Right:** Alkali silicate glass. The network of SiO_4 tetrahedra changes by alkali metal atoms. They reside in the structure, forming ionic bonds with the non-bridging atoms.

3.2.2 Phosphate glasses

Phosphate glass, with the chemical formula P_2O_5, has a SRO unit similar to that of silicate glass. They also form tetrahedral units[18]. The difference between silicon and phosphate is that phosphate has one electron more in its outer shell than silicon does. This means for the SRO unit that there is a double bond with one of the oxygen atom, while the rest of the oxygen atoms form single bonds (see Fig. 3.3). Thus the oxygen atom with the double bond now has a full outer shell and can't bond anymore. Therefore a Q^4 structural unit is not possible. This makes the Q^3 structural unit the most likely structure for pure phosphate glass. This theory was confirmed by neutron diffraction studies[19].

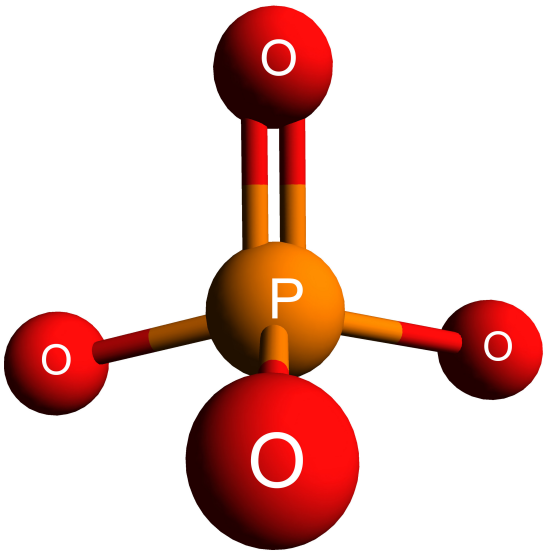

Figure 3.3: PO_4 tetrahedron

Adding alkali oxides to the glass has the same effect as for silicate glasses, namely the shift from Q^3 structural units to Q^2, Q^1 and Q^0 units. The proportion of different structural units for

$(A_2O)_x(P_2O_5)_{1-x}$ glasses, A being an alkali metal, depends on the fraction f of mole % of alkali oxides in the composition. This relation between the fraction of alkali oxides and structural units can be quantified[18], which is shown in Tab. 3.1.

Fraction of alkali oxide	f(Q_4)	f(Q_3)	f(Q_2)	f(Q_1)
$0 \leq x \leq 0.5$	0	$\frac{1-2x}{1-x}$	$\frac{x}{1-x}$	0
$0.5 < x \leq 2/3$	0	0	$\frac{2-3x}{1-x}$	$\frac{2x-1}{1-x}$
$2/3 < x \leq 0.75$	0	0	$\frac{3-4x}{1-x}$	$\frac{3x-2}{1-x}$

Table 3.1: The first column shows the fraction of an alkali oxide in the glass composition. The other columns show the fraction of the respective structural units as a function of x. In general, the number of bridging oxygen atoms decreases with increasing fraction of alkali oxides.

3.2.3 Borate glasses

Borate glass, with the chemical formula B_2O_3, has two different SRO units[20]. Pure borate glass has planar BO_3 triangles (see Fig. 3.4) as its SRO unit. The number of bridging oxygen is three, meaning that every oxygen atom is connecting two triangles with each other. The angles of the connections vary, making up a three-dimensional random network. By increasing the concentration of alkali oxides BO_3 tetrahedra (see Fig. 3.4) start forming.

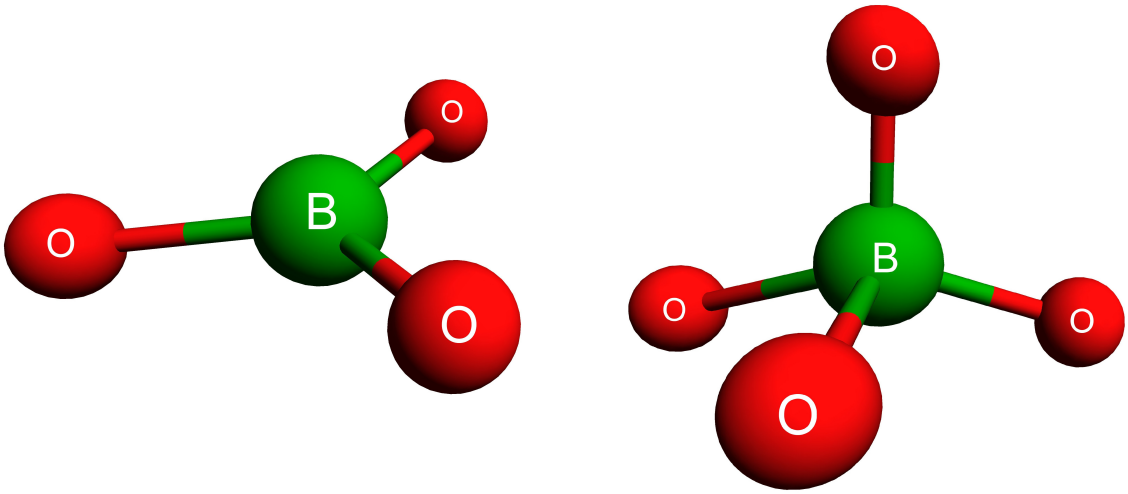

Figure 3.4: **Left:** Planar BO_3 Triangle **Right:** BO_4 tetrahedron

For low concentrations of alkali metals the fraction N_4 of BO_4 tetrahedrons is given by[21]

$$N_4 = \frac{x}{100 - x}. \tag{3.1}$$

While the number of BO_4 tetrahedrons rises, the fraction N_3 of triangular units decreases by

$$N_3 = \frac{100 - 2x}{100 - x}. \tag{3.2}$$

The number of BO_4 tetrahedrons increases up to an alkali concentration of about 30 mol %, depending on the specific alkali metal that is in the composition. Beyond that it decreases again, while the number of non-bridging oxygen atoms increases.

3.3 Glass transition temperature

Glasses are not in a thermodynamic equilibrium and thus don't exhibit a phase transition from liquid to solid. This implies there is no melting temperature T_m for glass and no latent heat that would occur at a phase transition. However, glasses experience a transition when heated up, called the glass transition. The according temperature is the glass transition temperature T_g. During this transition the glass goes from the typical hard and brittle into a viscous and rubbery state. This transition is completely reversible when the glass is cooled down again. However, there is a possibility of crystallization when the glass is heated above T_g. Whether the glass crystallizes or not depends on the specific conditions of the heating process and is different for every glass composition.

Unlike a first-order phase transition, the glass transition does not happen at a specific temperature, but over a small temperature range. There are two established methods to define T_g [16]:

1. One definition refers to the viscosity η. At the glass transition the viscosity $\eta(T_g)$ reaches 10^{12} Pa $\cdot$ s $= 10^{12}$ Nm^{-2}s $= 10^{13}$ poise.

2. There are several parameters of the material that show a relatively sudden change at the glass transition temperature. These are amongst others the thermal expansion and the heat capacity. This parameters can be used to determine T_g.

An example, using the heat capacity to determine T_g is shown in Fig. 3.5. In the example the inflection point is defined as T_g, which is a well justifiable definition since this is the point of maximal change of the heat capacity.

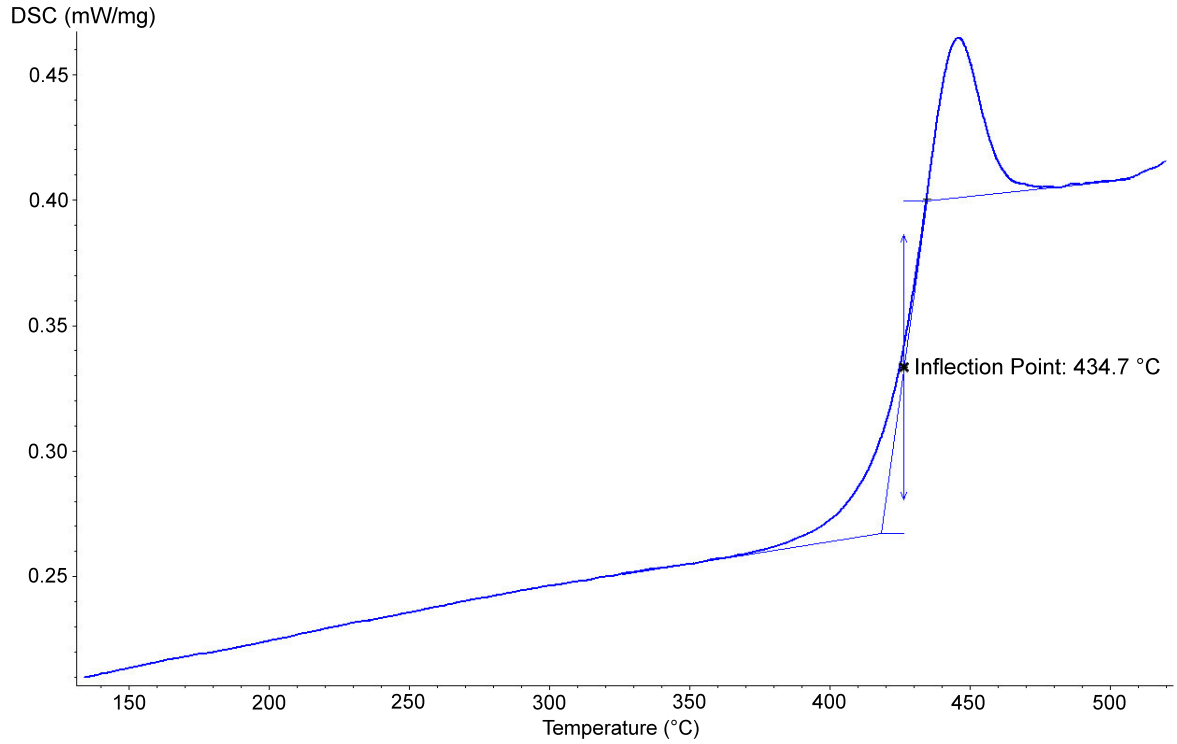

Figure 3.5: The heat capacity as a function of the temperature for a phosphate glass with the composition $(V_2O_5)_{50}(P_2O_5)_{50}$. At the glass transition there is a sharp change in the heat capacity, which is used to determine T_g.

It must be pointed out that the glass transition temperature depends on the heating rate and slightly changes when the rate is changed.

3.4 Dynamics in glasses

Today, it is widely believed that beneath the glass transition temperature, the glass forming network is in an arrested state. This means that the atoms are caught in a complex potential energy landscape where they cannot move freely anymore. The concrete form of the energy landscape is not only depending of the composition of the glass, as it would be the case in crystalline materials, but also of the thermal history. This means, that the energy landscape is unique for every glass.

Far beneath the glass transition temperature [1] most atoms have not the energy to surpass the potential wells they are caught in. They mainly move by vibrating within the well around their equilibrium position. Hence, the diffusion is very low. When they are able to pass the potential energy barrier, the movement is assumed to be very fast, almost like an instantaneous jump. The higher the temperature is, the more likely this jumps are, because the atoms have more energy at higher temperatures. These conceptions of the mechanism of diffusion in glasses form the basis of the jump diffusion model by Chudley and Elliott, that has been introduced in section 2.4.

The assumptions for the Chudley-Elliott model[9] in their most general form are:

- Atoms stay at a fixed position most of the time. Their mean residence time is τ_0.
- The jumps are isotropic, i.e. jumps are equally likely for all possible directions
- The jump length is given by a distribution $\rho(l)$.

Under this assumptions, the decay parameter $\Gamma(\mathbf{q})$ can be given in an analytical form[2]:

$$\Gamma(q) = \frac{1}{\tau_0}\left(\frac{\int_0^\infty (1 - \frac{\sin(ql)}{ql})\rho(l)dl}{\int \rho(l)dl}\right) \tag{3.3}$$

Here, q is the absolute value of the wave vector $\mathbf{q}$. Due to the isotropy of the jumps, the decay parameter only depends on the absolute value instead of the wave vector itself. τ_0 is the mean residence time, i.e. the average time an atom stays at its position. Furthermore, l is the jump length, which is described by the jump length distribution $\rho(l)$. If $\rho(l)$ is normalized, Eq. (3.3) can be rewritten as

$$\Gamma(q) = \frac{1}{\tau_0}\left(1 - \int_0^\infty \frac{\sin(ql)}{ql})\rho(l)dl\right). \tag{3.4}$$

To develop a concrete model, which can be compared to experimental data, the jump length distribution $\rho(l)$ needs to be specified. Some specific models are introduced and described below.

[1] For all glasses studied in this thesis, room temperature can be considered as far beneath glass transition temperature.

[2] A detailed derivation is given in the work of Ross[8].

3.4.1 One-jump Chudley-Elliott model

The simplest way, that is also the model presented in the original work of Chudley and Elliott, to specify $\rho(l)$ is by assuming, that there is only one fixed jump length l_1. Then the jump length distribution is given by a delta distribution:

$$\rho(\mathrm{l}) = \delta(\mathrm{l} - \mathrm{l}_1) \tag{3.5}$$

Inserting the distribution into Eq. (3.4) gives the decay parameter

$$\Gamma(q) = \frac{1}{\tau_0}\left(1 - \frac{\sin(ql_1)}{ql_1}\right). \tag{3.6}$$

3.4.2 Two-jump Chudley-Elliott model

A straightforward way to extend the one-jump model is to go to a linear combination of two different jump lengths:

$$\rho(l) = \omega_1\delta(l - l_1) + \omega_2\delta(l - l_2) \tag{3.7}$$

Here, the ω_i are the probabilities for their respective jump lengths $\mathrm{l_i}$, with $\omega_1 + \omega_2 = 1$. This gives the following decay parameter:

$$\Gamma(q) = \frac{1}{\tau_0}\left(1 - \omega_1\frac{\sin(ql_1)}{ql_1} - (1 - \omega_1)\frac{\sin(ql_2)}{ql_2}\right) \tag{3.8}$$

The model can also easily be extended to n ($\mathrm{n} \in \mathbb{N}$) different jump lengths.

3.4.3 Uniformly distributed jumps

Another approach is by using a uniformly distributed jump length distribution instead of a concrete number of fixed jump lengths. For this approach, $\rho(l)$ is defined as

$$\rho(l) = \begin{cases} \frac{1}{l_{\mathrm{max}}} & 0 < l < l_{\mathrm{max}} \\ 0 & \text{otherwise} \end{cases}. \tag{3.9}$$

Here, l_{max} is the maximal possible jump length. This distribution gives the following decay parameter:

$$\Gamma(q) = \frac{1}{\tau_0}\left(1 - \frac{1}{l_{\mathrm{max}}}\frac{\mathrm{Si}(ql_{\mathrm{max}})}{q}\right) \tag{3.10}$$

Si(x) in above equation is the Sine integral[3].

[3]The Sine integral is defined as following: $\mathrm{Si}(x) = \int_0^x \frac{\sin(t)}{t}dt$

3.4.4 Jobic model

The last model that will be introduced here is the Jobic model[22]. In this model $\rho(l)$ is defined as

$$\rho(l) = \frac{l}{d_0 r_0 \sqrt{2\pi}} \cdot \exp\left(- \frac{(l - d_0)^2}{2r_0^2} \right), \tag{3.11}$$

with d_0 being the mean value of the jump length and r_0 is the delocalisation of an atom from its site. This distribution gives the decay parameter

$$\Gamma(q) = \frac{1}{\tau_0} \left(1 - \frac{\sin(qd_0)}{qd_0} \cdot \exp\left(- \frac{q^2 r_0^2}{2} \right) \right). \tag{3.12}$$

Chapter 4

Experimental approach

A crucial part of any experiment is the preparation of the samples. This is especially true for aXPCS experiments where the samples have to be very thin to meet experimental demands. Ideally the sample thickness is close to the optimal scattering thickness and thinner than the longitudinal coherence length. How the samples were prepared will be shown in this chapter in detail.

4.1 Sample preparation

4.1.1 Mixing

The first step was to produce the different glass compositions. The aim was to have several compositions of alkali borate and alkali silicate glasses prepared for the measurements at the synchrotron radiation facilities. The alkali borate glasses had already been produced due to their use in previous experiments. They only had to be grinded and dimpled for optimal thickness.

The alkali silicate glasses had to be produced from scratch. The raw materials were delivered in powder form. The main component and network former SiO_2 came in pure form. The alkali metals, i.e the network modifiers, came in form of carbonates, e.g. Rubidium carbonate with the chemical formula Rb_2CO_3. In the course of the melting process the chemical reaction

$$Rb_2CO_3 \Longrightarrow CO_2 + Rb_2O$$

occured and the CO_2 evaporated. This reaction and loss of mass occurs for all alkali metals and has to be considered when calculating the mass of raw materials needed. To achieve this one has to multiply the mass with the gravimetric factor (GF)[23]

$$\text{GF} := \frac{\text{Mass of raw material}}{\text{Mass of the glass component}} \tag{4.1}$$

In the next step the raw mass needed for the i-th glass component A_i with a fraction of x (mole %) of a glass batch can be calculated using the equation

$$(\text{Mass of raw material for } A_i) = (\text{Mass of batch}) \cdot \frac{x \cdot (\text{Molecular mass of A})}{(\text{Molecular mass of } (A_1)_{x_1} ... (A_n)_{x_n})} \cdot \text{GF} \tag{4.2}$$

After weighting the components with an accuracy of 0.001 g they have been mixed together in a mortar to reach a homogeneous powder.

Example: mixing process

In this example the amount of raw materials needed for a 15 g batch of $(Rb_2O)_{10}(SiO_2)_{90}$ will be calculated.

The first component, SiO_2, already comes in this chemical composition. Hence, according to Eq. (4.1),

$$GF = 1.$$

Therefore, Eq. (4.2) gives

$$\text{Mass of raw material for } SiO_2 = 15 \text{ g} \cdot \frac{0.9 \cdot 60.08 \text{ u}}{0.9 \cdot 60.08 \text{ u} + 0.1 \cdot 186.93 \text{ u}} \cdot 1 = 11.147 \text{ g}$$

The second component, Rb_2O, comes in the carbonated form Rb_2C0_3. Hence, according to Eq. (4.1),

$$GF = \frac{230.94 \text{ u}}{186.93 \text{ u}} = 1.24.$$

Therefore, Eq. (4.2) gives

$$\text{Mass of raw material for } Rb_2O = 15 \text{ g} \cdot \frac{0.1 \cdot 186.93 \text{ u}}{0.9 \cdot 60.08 \text{ u} + 0.1 \cdot 186.93 \text{ u}} \cdot 1.24 = 4.761 \text{ g}$$

4.1.2 Melting

Three furnaces were used in the process of glass making. The first furnace was a self-made furnace. It has an open top and can heat up to around 1100 °C. Since silicate glasses have a very high melting point, e.g. pure SiO_2 has a melting point of 1713 °C[24], this furnace was not suitable for fully melting the glass. However it was sufficient to heat to temperatures high enough to start the glass forming chemical reaction in which the CO_2 evaporates. By constantly stirring the mixture it was possible to have most of the CO_2 evaporate. The remaining CO_2 in the melt formed bubbles. The mixture was then fast cooled to room temperature. In the next step the crucible with the mixture was put in the second furnace. This one was a closed system and stirring was not possible, hence the importance of the first furnace. The maximum temperature was 1500 °C and enough to fully melt all compositions of alkali silicate glasses. The melt was in this furnace for a couple of hours to make sure all remaining bubbles in the glass were removed. The mixture was then cooled as slow as possible to room temperature to avoid cracks caused by internal stresses.

4.1.3 Measuring the glass transition temperature

The glass transition temperature T_g was measured using a Differential Scanning Calorimeter[1]. All measurements were conducted with a heating rate of 20 K/min and a cooling rate of 10 K/min. The results are shown in Tab. 4.1). T_g was needed for two reasons. Firstly, it was needed for the annealing that follows the melting process. Secondly, the glass transition temperature was needed later to correctly interpret the results of the aXPCS experiments.

[1] Netzsch DSC 204 Phoenix

Sample	T_g	Sample	T_g
$(Na_2O)_{10}(SiO_2)_{90}$	597.9 °C	$(B_2O_3)_{100}$	292.4 °C
$(Na_2O)_{40}(SiO_2)_{60}$	566.0 °C	$(Li_2O)_{20}(B_2O_3)_{80}$	487.3 °C
$(Rb_2O)_{10}(SiO_2)_{90}$	514.2 °C	$(Na_2O)_5(B_2O_3)_{95}$	355.3 °C
$(Rb_2O)_{15}(SiO_2)_{85}$	455.9 °C	$(Ka_2O)_{20}(B_2O_3)_{80}$	446.7 °C
$(Rb_2O)_{15}(Li_2O)_{15}(SiO_2)_{70}$	521.0 °C	$(Rb_2O)_2(B_2O_3)_{98}$	314.0 °C
$(PbO)_{30}(SiO_2)_{70}$ [8]	479.9 °C	$(Rb_2O)_{15}(B_2O_3)_{85}$	400.1 °C
$(V_2O_5)_{50}(P_2O_5)_{50}$	434.7 °C	$(Cs_2O)_2(B_2O_3)_{98}$	322.8 °C
$(V_2O_5)_{75}(P_2O_5)_{25}$	275.9 °C	$(Cs_2O)_{15}(B_2O_3)_{85}$	382.5 °C

Table 4.1: Glass transition temperature measured with a DSC for all compositions of silicate and vanadium glasses produced as well as all other glasses used for aXPCS measurements. Only the value for the lead glass was not measured, but taken from literature instead.

4.1.4 Annealing

The internal stresses are caused by the complex potential energy landscape in glass due to the fact that it is not in a thermodynamic equilibrium. When glass is cooled down fast there is not enough time for the atoms to rearrange and to level out this internal stresses.

Annealing is the process of slowly cooling glass down to relieve internal stresses. The process should start at a temperature T_a that is slightly beneath the glass transition temperature T_g. Above T_g there is a certain risk that the material starts to crystallize. To far beneath T_g the annealing becomes less efficient and more time consuming. The temperature T_a should be held for a couple of hours and then the glass should slowly be cooled down to room temperature. The result of the process is a less brittle glass than it would be without annealing.

For the annealing process a third furnace was used. This furnace was electrically powered and programmable. The beforehand produced batches of glass were heated up to the annealing temperatures T_a slightly beneath glass transition temperature, held at T_a for a couple of hours and then cooled down again slowly to room temperature.

4.1.5 Grinding and dimpling

After the glass is produced and annealed it needs to be cut and grinded until it the optimal thickness is reached. Mainly two factors determine the optimal thickness of a sample in an aXPCS experiment.

The first factor is the sample thickness that maximizes the scattered intensity for a given scattering angle θ and an absorption coefficient μ [8] (see Appendix A for the derivation)

$$W(\theta, \mu) = \frac{\ln(\cos(2\theta))}{\mu(1 - \frac{1}{\cos(2\theta)})} \tag{4.3}$$

For $\theta = 0$, Eq. (4.3) reduces to

$$W(\theta = 0, \mu) = \frac{1}{\mu} =: \lambda. \tag{4.4}$$

This is the attenuation length λ of a given material. It depends on the materials composition, density and the wavelength of the incoming beam. The attenuation lengths were obtained from an

X-ray database[2]. Densities, used in the calculation, were either measured by ourselves[3] or gained from literature. Table 4.2 gives an overview over all samples including their density and attenuation lengths.

Since $W(\theta, \mu)$ is monotonically decreasing in θ it reasonable to take Eq. (4.4) as an upper bound for the sample thickness.

Sample	Density (g/cm^3)	λ (μm) for ESRF	λ (μm) for PETRA III
$(Na_2O)_{15}(SiO_2)_{85}$	1.957 $\pm$ 0.445	159.79	650.70
$(Na_2O)_{40}(SiO_2)_{60}$	2.552 $\pm$ 0.036	133.64	547.55
$(Rb_2O)_{10}(SiO_2)_{90}$	2.769 $\pm$ 0.096	75.57	292.50
$(Rb_2O)_{15}(SiO_2)_{85}$	2.727 $\pm$ 0.073	68.95	263.95
$(Rb_2O)_{15}(Li_2O)_{15}(SiO_2)_{70}$	2.828 $\pm$ 0.021	70.46	269.09
$(PbO)_{30}(SiO_2)_{70}$	4.46 [25]	13.22	45.78
$(V_2O_5)_{50}(P_2O_5)_{50}$	2.810 $\pm$ 0.005	40.05	150.78
$(V_2O_5)_{75}(P_2O_5)_{25}$	2.923 $\pm$ 0.020	31.11	116.08
$(B_2O_3)_{100}$	1.830 $\pm$ 0.002 [26]	669.83	2851.19
$(Li_2O)_{20}(B_2O_3)_{80}$	2.117 $\pm$ 0.003 [23]	594.18	2524.87
$(Na_2O)_5(B_2O_3)_{95}$	1.984 $\pm$ 0.002 [23]	564.13	2397.24
$(K_2O)_{20}(B_2O_3)_{80}$	1.990 $\pm$ 0.002 [23]	135.88	520.89
$(Rb_2O)_2(B_2O_3)_{98}$	1.979 $\pm$ 0.002 [23]	409.13	1645.85
$(Cs_2O)_2(B_2O_3)_{98}$	1.929 $\pm$ 0.005 [23]	169.85	630.60
$(Cs_2O)_{15}(B_2O_3)_{75}$	2.544 $\pm$ 0.006 [23]	28.22	101.10

Table 4.2: All samples that were prepared for measurements at the synchrotron. There are two columns for the attenuation lengths. This is, because the photon energies at ESRF (8.1 keV) and PETRA III (13 keV) were different. The densities were either measured or taken from literature.

The second factor that needs to be taken account for is the coherence of the beam. Eq. (2.8) gives a condition for the maximal path length difference P. This inequality can be rearranged, so that it provides an upper bound for the sample thickness:

$$\mathrm{W} \leq \frac{\xi_l - d \cdot \sin(2\theta)}{2 \cdot \sin^2(\theta)} \tag{4.5}$$

At beamline ID10, ESRF, a Silicon (111) crystal pseudo channel cut is used as a monochromator. Its spectral resolution $\lambda/\Delta\lambda = 1.4 \cdot 10^{-4}$. This gives a longitudinal coherence length $l_l = 0.54$ μm. The diameter of the beam is approximately 10 μm. For a value of $2\theta = 10°$, the upper bound for the sample thickness W = -78.75 μm, according to Eq. (4.5). Of course, a negative value for a thickness is not possible. The physical meaning of this is that for the setup at ESRF, full coherence is not possible. This is furthermore true for all possible angles at ESRF, as well as for the setup at PETRA III.

The consequence of this is, that on the one hand, the sample should be as thin as possible to achieve a high degree of coherence. On the other hand, attenuation lengths for achieving maximal scattering vary greatly between approximately 13 μm and 2851 μm. Since it is impossible to gain any information without contrast, the decision was made, to make all samples around 50 μm thick.

[2] http://henke.lbl.gov/optical_constants/atten2.html (January 23, 2018)

[3] The densities were measured by using Archimedes' method [23].

Thinner was not possible to the brittle nature of glass, otherwise too many samples would have been destroyed during production.

Technically, this was achieved by grinding all samples to a thickness of 200 μm at first using a standard flat grinder. For stability reasons the final thickness of 50 μm was achieved using a dimple grinder. Its spherical geometry made it possible to achieve the final thickness while maintaining a high degree of stability in comparison to a standard flat grinder.

4.2 Sample environment for aXPCS measurements

4.2.1 Prerequisites

Some of the samples, in particular the borate glasses, showed hygroscopic properties. To avoid chemical reactions on the surface of the samples, all were stored in a dry environment. Furthermore each sample was stored in a plastic box with an inbuilt membrane that secured that glass from breaking during transport and storage.

4.2.2 Requirements

An aXPCS experiment at a synchrotron has two main requirements to the sample environment. The uttermost important one is that the sample is in high vacuum. Otherwise the scattering of the beam in air would overshadow the scattering of the sample by several orders of magnitude and only noise would be seen at the detector.

Secondly, the temperature must be stable and tunable. Internal diffusion is a thermally activated process. A change in temperature during the measurement would therefore distort the results of the measurements. This makes a stable temperature very important.

Furthermore one wants to measure the diffusion at temperatures different from room temperature. For this purpose the sample environment should also be able to heat and cool the sample.

4.2.3 Vacuum chamber

A self-made vacuum chamber was used for the measurements at the synchrotron. It is shown in Fig. 4.1.

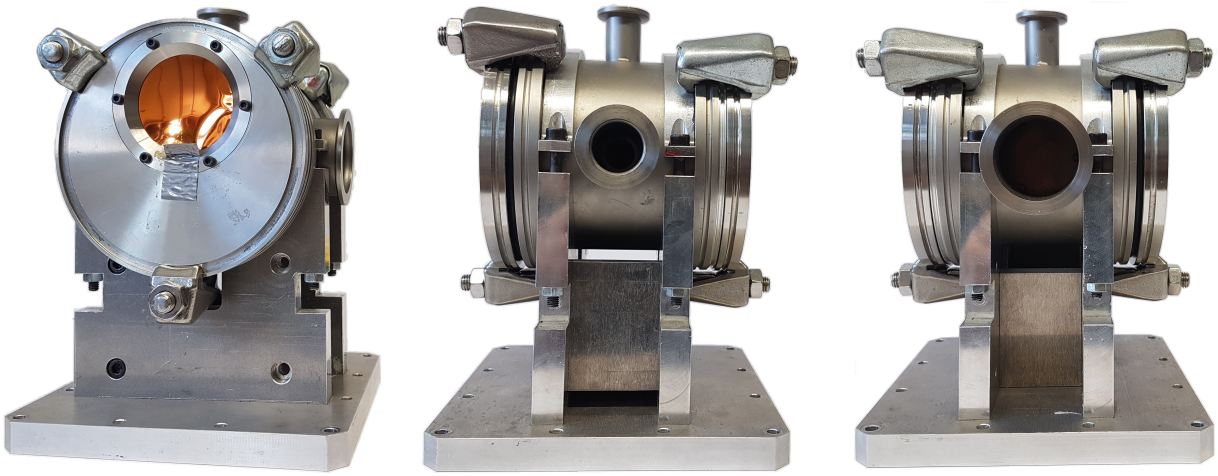

Figure 4.1: **Left:** Front view of the vacuum chamber. It shows the window were the X-ray beam leaves the chamber. The front window as well as the rear window are made out of Kapton. This material has high mechanical and thermal stability and its high transmittance to X-rays makes it the optimal material for X-ray experiments. Beneath the front window a lead strip can be seen. It was used to block the main beam from exposing the detector. **Middle:** Side view of the chamber with the opening for the sample holder. **Right:** Side view of the chamber with the opening for the vacuum tube. At the top of the device the opening for the electrical connection can be seen.

The chamber is build for measuring in a temperature range from 150 K to 1300 K[8]. To cover such a broad temperature range two different sample holders exist (see Fig. 4.2), one for measuring at room temperature and heating the sample and a cold finger for the cooling mode:

- Heating Mode
  For the heating mode the standard sample holder is used. When inserted into the vacuum chamber the sample is in the middle of a resistive heating furnace, which is build in to the chamber. The heating wires are made of tantalum with 0.25 mm diameter.

- Cooling Mode
  For cooling below room temperature a self-made cold finger is in use. It has a cooling pipe and a Peltier element for cooling. When used with water, the cooling pipe is for basic cooling and conducting heat out of the cold finger. The Peltier element runs with a maximal power of 20 W and a maximal temperature difference of $\Delta T \approx 75$ K. For cooling down even further the cooling pipe can be used with liquid nitrogen instead of water. Then temperatures of around 150 K can be reached.

Figure 4.2: **Left:** Standard sample holder for measuring at room temperature and for heating the sample. **Right:** Cold finger for measuring in cooling mode.

In the course of this thesis, only measurements at and above room temperature have been made. Hence only the standard sample holder was in use. A problem was the brittleness of the glass samples. It was not possible to mount them in the sample holder directly, which consists of a hard metal, without breaking them. To still be able to mount it, leaflets made out of Boron nitride had been placed between the sample holder and the glass samples.

4.2.4 Synchrotron setup

All data presented in this thesis have been obtained at two beamtimes. The first beamtime was in April, 2017 at PETRA III, Hamburg. It lasted 5 days. The second beamtime followed immediately in May, 2017 at ESRF, Grenoble and lasted 7 days.

All measurements were performed with the sample in the vacuum chamber described above. The air pressure inside the chamber was kept as low as possible and reached values around 10^{-6} mbar. At both synchrotrons a variety of measurements was performed, i.e. different glass compositions at different temperatures and different angles 2θ.

PETRA III, Hamburg

Measurements at the DESY (**D**eutsches **E**lektronen **Sy**nchrotron) research facility in Hamburg were carried out at PETRA III, a 3rd generation synchrotron[4]. In 2017 it was the largest and brightest synchrotron light source in the world with a circumference of 2.3 km and a brilliance exceeding 10^{21} ph /(s mm^2 mrad^2 0.1% BW). PETRA III ran at 100 mA beam current in top-up mode [5], keeping the photon flux stable with maximal fluctuations in the order of 1%.

All measurements were conducted at the coherence applications beamline P10. It serves three experimental goals:

- X-ray Photon Correlation Spectroscopy (XPCS)
- Coherent diffractive imaging of micro- and nanostructures (CDI)
- Time-resolved SAXS studies of complex liquids (Rheo-SAXS).

The beamline operates in the medium-hard X-ray regime from 3.8 keV to 10.5 keV and 11.4 keV to 25.0 keV. Our measurements at PETRA III were all carried out at a fixed energy of 13 keV. The beam was monochromatized by a cryocooled double crystal monochromator crystals (Si(111) and Si(111) channelcut) with a spectral resolution $\Delta\lambda/\lambda$ in the order of 10^{-5}.

The total photon flux was not measured and is unknown. Hence we were only able to compare relative fluxes within one synchrotron. To reduce the flux of the beam, up to four Si(111) single crystalline foils were used. One Si(111) crystal reduced the flux by a factor of 2.07.

The detector used at PETRA III was a Dectris Eiger X area detector. It consisted of eight separate modules with a total number of 2070 x 2167 Pixel. According to Eq. (2.18) the contrast scales with the square root of the number of pixels. This is a tremendous advantage in comparison to a point detector. The detector had a dead time[6] of 3 μs and works in continuous readout time modus.

[4] Information received from *http://photon-science.desy.de/facilities/petra_iii* (January 23, 2018)

[5] Top-up is a way of injecting electrons into the storage ring. This mode sees the accelerator refilled with electrons constantly rather than every couple of hours. This results in a much higher integrated current over a 24-hour period and also provides a higher stability in the intensity of the beam.

[6] The dead time is the time after each photon event during which a pixel of the detector is not able to record another photon.

Both, the short dead time and the continuous readout time, allowed for very fast measurements. A single frame irradiation at PETRA III took about 0.1-1 s as opposed to a measurement at ESRF, where it took about 3-5 s. The detector had a tunable energy threshold[7], ranging from 2.7-18 keV.

The experimental hutch, including the already mounted vacuum chamber and the detector are shown in Fig. 4.3.

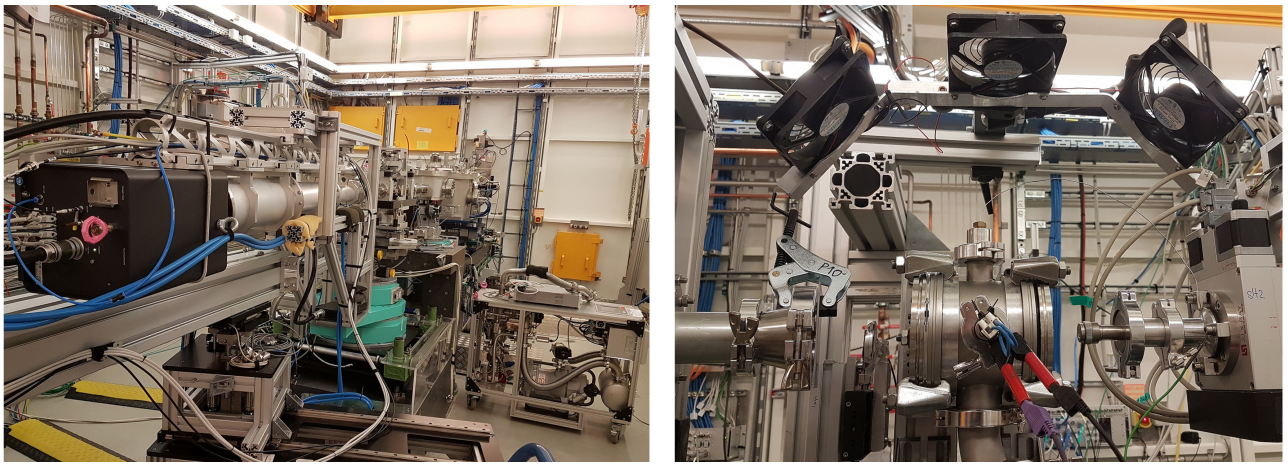

Figure 4.3: **Left:** The experimental hutch at beamline P10. The detector can be seen on the left side in the middle (black box). **Right:** The vacuum chamber mounted in the experimental hutch. The beams goes from right to left. Due to technical reasons the chamber was not standing, but hung up on the side. This is why the electric connection appears to be on the side of the chamber. Three ventilators were mounted above the vacuum chamber. The were switched on as long as the sample was heated. It was necessary to keep the outer shell of the chamber as cool as possible, since some parts of it are not heat-resistant.

ESRF, Grenoble

The synchrotron at ESRF (**E**uropean **S**ynchrotron **R**adiation **F**acility), Grenoble has a circumference of 844 m and is, like PETRA III, a 3^{rd} generation synchrotron[8]. The beam current was 200 mA at maximum. It got refilled with electrons every 12 hours. This makes the beam flux less stable compared to a synchrotron running in top-up mode. All measurements were conducted at the beamline ID10, EH2. This beamline is specialized for XPCS, Coherent X-ray Diffraction Imaging (CXDI) and surface scattering techniques.

The beamline operates in an energy range of 7.0 - 24.0 keV. All measurements at ESRF were carried out at a fixed energy of 8.1 keV. The beam was monochromatized by a Si(111) crystal with a spectral resolution of $\Delta\lambda/\lambda = 1.4 \cdot 10^{-4}$. Similar to the situation at PETRA III, the total photon flux was not measured and is unknown as well. Hence we were only able to compare relative fluxes. To change the flux of the beam up to four Si(111) oriented crystal were used. Each Si(111) crystal reduced the flux by a factor of $e \approx 2.71$.

The detector used at ESRF was an Andor CCD camera with 1024 x 1024 Pixel and a pixel size of 13 x 13 μm.

The experimental hutch, including the already mounted vacuum chamber and the detector are shown in Fig. 4.4.

[7]The energy threshold is a lower limit for the energy of photons detected as a photon event.
[8]Information received from *http://www.esrf.eu/about/synchrotron-science* (January 23, 2018)

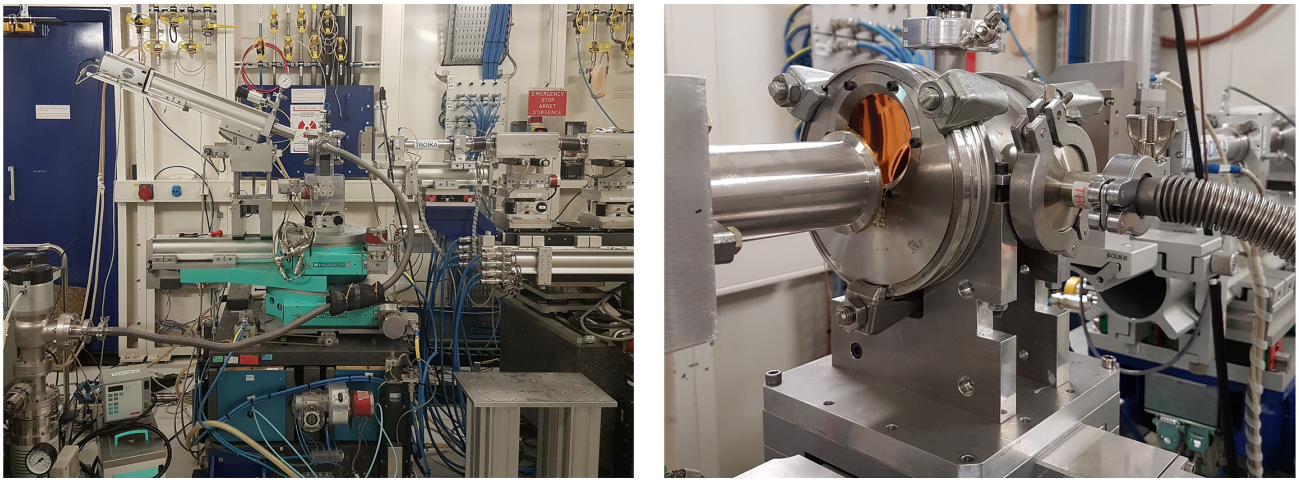

Figure 4.4: **Left:** The whole setup shown from the side at the experimental hutch at beamline ID10, EH2. The detector can be seen on the left upper side. **Right:** The vacuum chamber (in front view) mounted in the experimental hutch. The vacuum chamber is standing upright. The electrical connection is seen on top and the vacuum tube on the right side of the chamber.

Chapter 5

Data evaluation and analysis

The raw data gained during the experiments needs to be processed further in order to gain information on the beam-induced dynamics in the samples. The data evaluation consists mainly of two steps.

Firstly, the autocorrelation function (Eq. 2.17) must be calculated for each measurement. The calculation differs for the data evaluated at the ESRF and PETRA III. The reason for this is the fact that the two synchrotrons had different detectors and they used different data formats. The process of data evaluation for both is described in this chapter in detail.

Secondly, the functional form of the ACF (Eq. 2.19) must be fitted to the data points of the experimentally gained ACF that was calculated in the first step. The second step is independent of the synchrotron the data was gained from.

5.1 Evaluation at ESRF

5.1.1 Saving the frames

The first step is to save the data. The Andor CCD camera used at ESRF saves all data in the European Data Format (EDF). It is a standard file format designed for exchange and storage of time series. It saves every time frame acquired in its own file, e.g. a measurement of a thousand time frames consists of a thousand EDF files. Once all the frames are saved, several more steps need to be taken to bring the data in the form needed.

5.1.2 Subtracting dark current

A CCD camera consists of an array of photosensitive capacitors. Each capacitor acts as one pixel of the detector. When a photon hits the detector it is creating a cloud of electric charges. The intensity of the cloud is dependent on the photon energy, making the detector energy sensitive. An ideal detector would only record electric current in the case of a photon event. However, in a real experiment the situation is more complicated, since there is current flowing without the detector being illuminated by photons. The dark current is due to the random generation of electrons and holes within the depletion region of the device. The effect increases with higher temperature[27]. As long as the environment of the camera, especially the temperature, is stable during a measurement, the dark current is time independent. A software algorithm, developed in our research group, was used to subtract the dark current from each frame.

5.1.3 Histogram

During readout the detector converts the electric charges to ADUs (Analog-to-digital units). The number of ADUs for a photon event depends on the energy of the photon. aXPCS is an elastic scattering technique, therefore the ADUs corresponding to the elastic photon events are needed. An elastic photon at ESRF had an energy of 8 keV, which corresponded to around 2000 ADUs. Other events like fluorescence in the sample or the Si escape peak[28] within the detector correspond to a different and lower number of ADUs. An algorithm is used to generate a Histogram (see Fig. 5.1) that plots the number of ADUs against the number of counts. The elastic peak must be the largest peak. Otherwise too much fluorescence or other undesirable events are occurring, making an evaluation of the ACF impossible. When calculating the autocorrelation function one wants to only take the elastic photons into account and neglect all other photons. To do that a small range in the elastic regime is chosen for all further calculations.

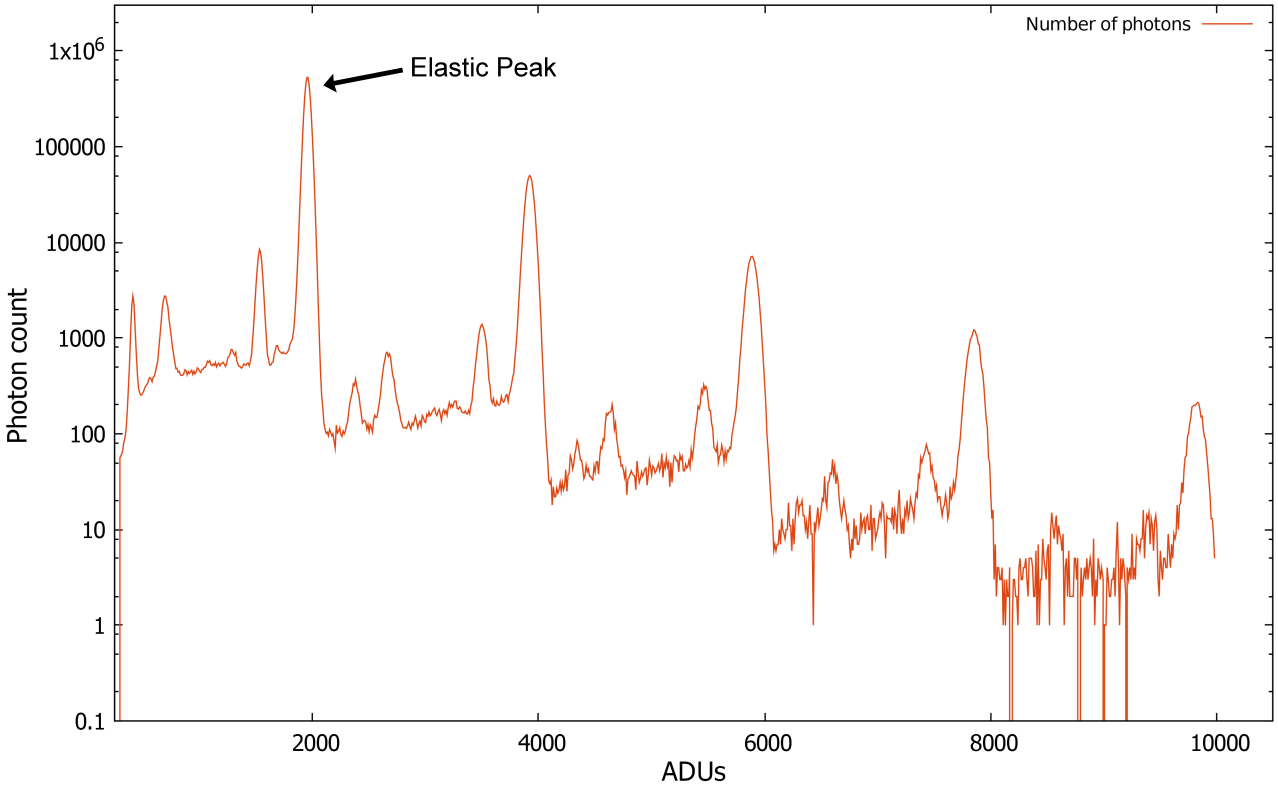

Figure 5.1: Histogram for a $(PbO)_{30}(SiO_2)_{70}$ sample, measured at ESRF. The x-axis is plotted in a linear scale, while the y-axis is in a logarithmic scale. Here, the elastic peak is the peak with the most counts at around 2000 ADUs. The peaks left of the elastic peaks are inelastic peak and must be neglected, since they only contribute noise to the ACF. A detailed analysis of inelastic peaks is given in the work of Leitner[1]. The peaks right to the elastic peaks account for multiple photon events, including again elastic and inelastic photon events. Since the intensity of the multiple photon events are only a fraction of the single photon events, they can be neglected.

5.1.4 Droplet algorithm

The charge cloud that is created by an incident photon is in general spread over multiple pixels. The purpose of the droplet algorithm is to identify the position and energy of the incident photons. This is the last step before the autocorrelation function can be calculated.

It is also important that the intensity at the detector is quite low, so that there are as few multiple photon events as possible. This has two reasons. Firstly, the software was written in such a way that it can only handle single photons events. This is due to the fact that treading the data as binary makes the computation significantly faster[8]. Secondly, it would be difficult and in some cases impossible to separate position and energy of these photons. During all our measurements the ratio of photons/pixel for a given frame was around 1%, so the probability for two-photon events was only 10^{-4} and could be neglected.

5.1.5 Autocorrelation function

After the droplet algorithm is carried out each pixel of each frame is now assigned with zero or one photon event. As mentioned before, multi-photon events will be ignored and also assigned with one photon event. In the last step, the autocorrelation function 2.17 is evaluated. The data of the ACF is then saved in a simple text file.

5.2 Evaluation at PETRA III

5.2.1 Saving the frames

The data evaluation process at PETRA III differed significantly from the process at ESRF.

Firstly, the detector used at PETRA III, an Eiger 4M from Dectris does not convert charge clouds into ADUs. It converts the charges directly in the detector into photon counts. The advantage of this method is that there are no dark counts that need to be subtracted and no droplet algorithm is needed. The disadvantage of this method is that the detector is not energy sensitive since every charge cloud gets converted directly into photon counts. However it is possible to define a threshold, so that photons with an energy less than the threshold do not get counted. This makes it possible to cut off typical fluorescence energies. One must be careful though, since a threshold also dismisses some elastic photons that are spread over more than one pixel. This can be a problem in the case that the intensity is low.

Secondly, the detector saves the time frames in the Hierarchical Data Format (HDF). This format is quite different from the EDF. The HDF was originally developed at the National Center for Supercomputing Applications, USA. It is designed for saving large amounts of data. In contrast to EDF, where every time frame is saved as a file, HDF saves all time frames in one file. Furthermore it saves all kind of metadata from the measurement, like incident photon energy, beam size etc. in the same file. The internal hierarchical structure of the HDF resembles the familiar folder structure of common operation systems. To browse and edit this internal structure, the HDF group provides the program HDFView (see Fig. 5.2).

Furthermore, the HDF files were compressed with the LZ4 compression algorithm. It is a lossless data compression algorithm focussing on compression and decompression speed.

Another software used at PETRA III was Albula (see Fig. 5.3). It is a program from Dectris to display and analyse image data from the Eiger detector. It consists of the standalone Albula Viewer

and the Python programming interface Albula API. The Albula Viewer (see. Fig. 5.3) is a fast and easy-to-use program that allows optimal visualization of data. It enables one to have a live view at the detector and the photons events occurring during a measurement.

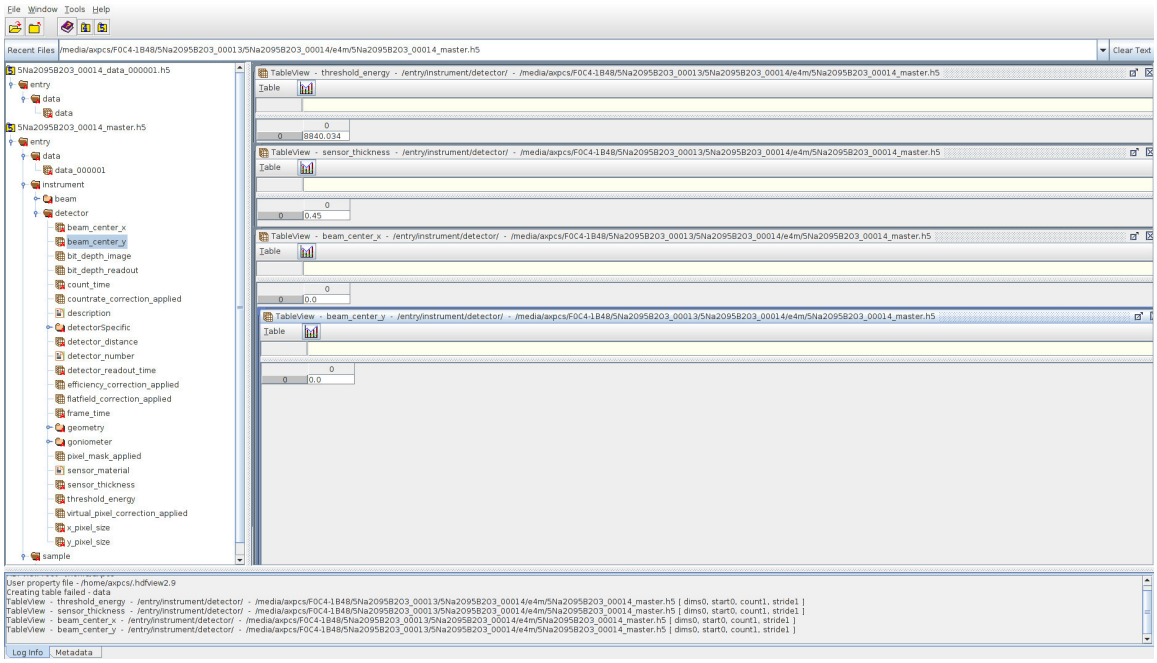

Figure 5.2: Screenshot of HDFView, provided by the HDF group. It is a visual tool for browsing and editing HDF files. It allows the user to enter all saved meta-data of a measurement with a view clicks, making it a very useful additional tool in data evaluation after an experiment.

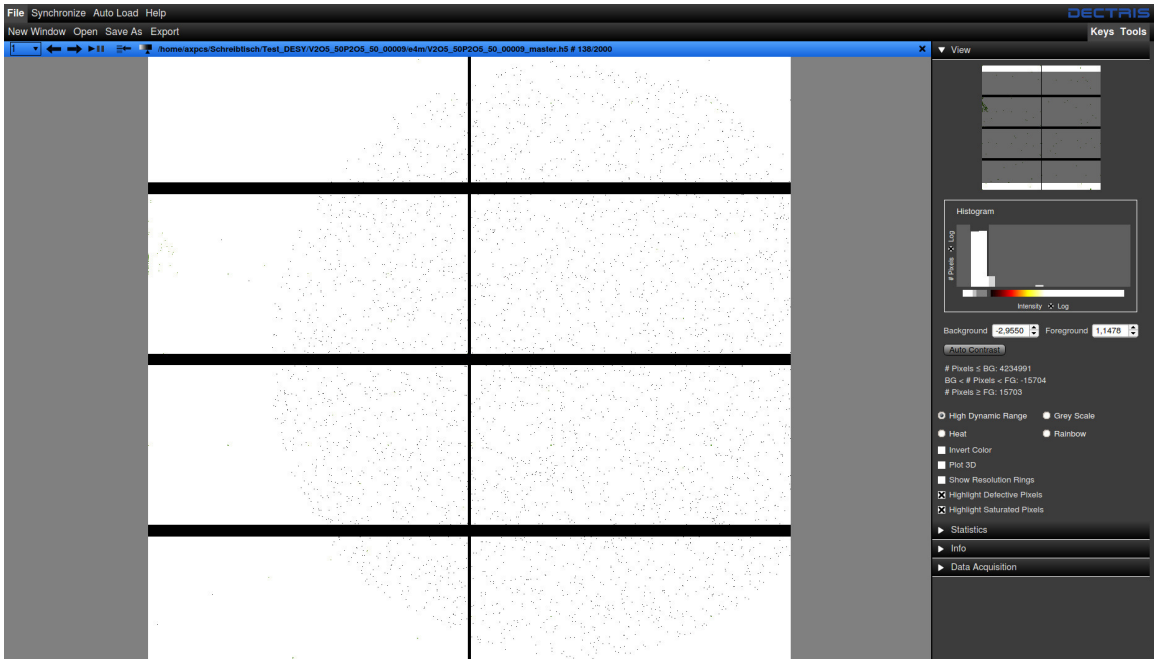

Figure 5.3: A screenshot of the Albula software. It shows the eight modules of the detector during a measurement. The black dots on the modules are photon counts.

5.2.2 Autocorrelation function

The autocorrelation function 2.17 can directly be calculated from the respective HDF-file, since it already contains the necessary data needed. And similar to ESRF, the data is then saved in a simple text file.

5.3 Logarithmic binning

A typical autocorrelation function is shown on the left side of Fig. 5.4. The x-axis is usually chosen to be in logarithmic scale. As can be seen in the plot, the values of the ACF scatter more and more the larger Δt becomes. This behaviour can be best understood by looking at Eq. (2.13). According to this equation, a data point gets calculated by averaging over all values with the same Δt. However, the larger Δt becomes, the less values are available to average over. Therefore, the statistics become worse the larger Δt becomes. To counterbalance this effect, a technique called logarithmic binning is used. There are several ways to implement it. The one that was implemented in this thesis works as following:
Firstly, a binning factor must be defined. Here, the binning factor was chosen to be 1.05. Then, beginning from the first data point, the i-th data point will be multiplied with the binning factor (bf). The result is rounded to the next natural number. Then the values from the i-th data point up to the round(i*bf)-th data point will be averaged. For example, the first data point multiplied with the binning factor gives 1 after rounding. This means that no averaging will be done. The 10-th data point multiplied with the binning factor gives 11 after rounding. Therefore, the 10-th and the 11-th data point will be averaged. And the 100-th data point will be already averaged up to the 105-th data point. It shows that the larger i is, the more data points are averaged and the worsening of the statistics can be counterbalanced this way.
A Matlab code for logarithmic binning is given in Appendix B.
An example for a data set before and after logarithmic binning is shown in Fig. 5.4.

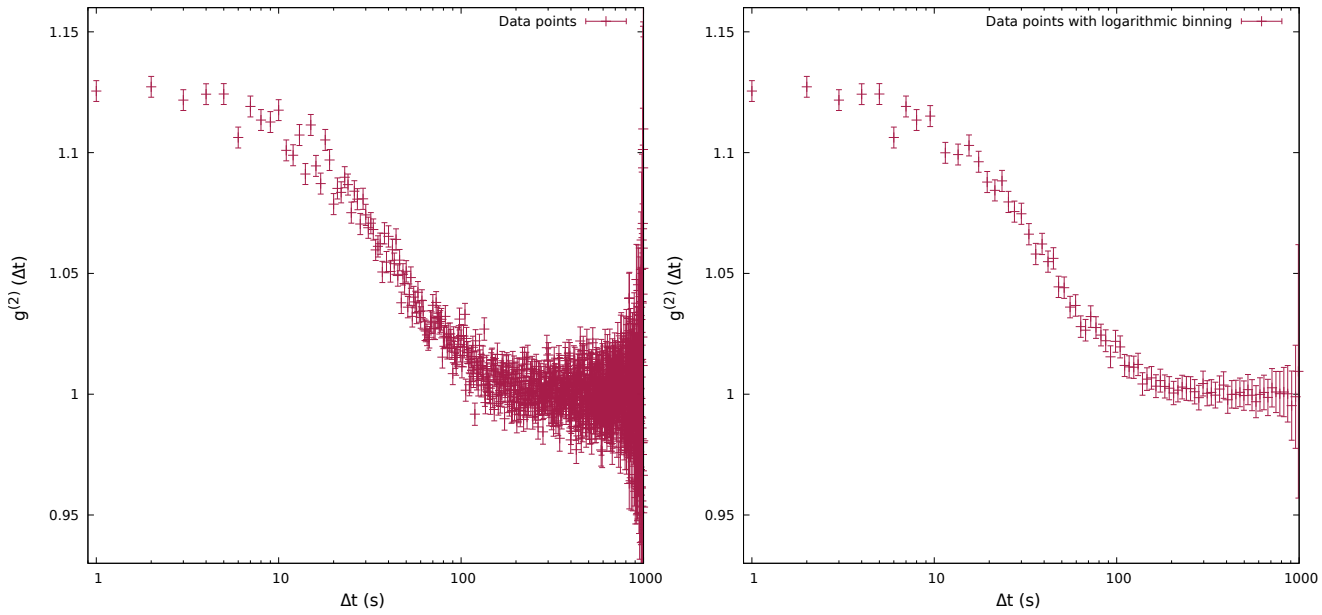

Figure 5.4: **Left:** Calculated autocorrelation function before logarithmic binning. **Right:** The same autocorrelation function after logarithmic binning.

One should stress that the binning procedure does not influence in any way the statistics of the measured data and only enhances the visibility of the data. Fitting of the left and right data sets in Fig. 5.4 provides the same correlation time and the same error bars.

5.4 Data analysis

To gain information about diffusion in a sample, the functional form of the ACF must be fitted to the data obtained in the previous step. To do this, a modified version of Eq. (2.19) is used:

$$g^{(2)}(\Delta t) = c_0 + \beta e^{-2(\frac{\Delta t}{\tau})^{\alpha}} \tag{5.1}$$

Firstly, during a measurement the detector is at a fixed angle 2θ. This means that the q-dependence of Eq. XYZ is not important for the data evaluation process of a single ACF and therefore $\Gamma = \frac{1}{\tau}$ is a constant here.

Secondly, there is the additional parameter c_0. This is necessary to adjust to experimental conditions. In an actual experiment the baseline does not exactly equal 1 as theory tells, but is usually slightly off resulting in a c_0 that is close to 1 but does not equal 1.

This parameter as well as the parameters α, β and τ must be fitted to the experimentally obtained data. The crucial parameter here are τ and α, since they contain all relevant information on the dynamics in a material. There are a variety of software packages that can be used for fitting and plotting the function. In the course of this thesis all calculations and plots were done with gnuplot.

A typical example of a function that is fitted to the experimental data is shown in Fig. 5.5.

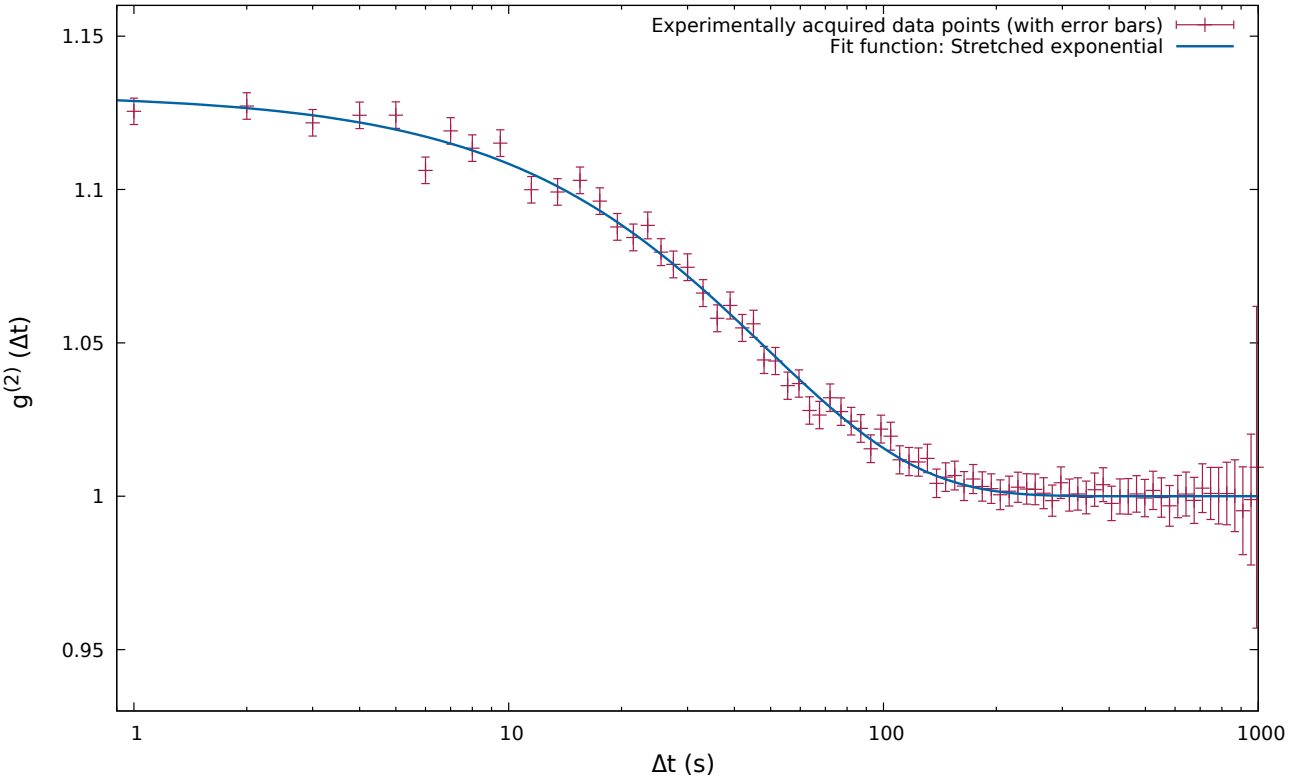

Figure 5.5: Stretched exponential function fitting the experimentally gained autocorrelation function. The x-axis is usually chosen to be logarithmic, so the decline of the exponential function can be seen better.

Chapter 6

Results

In this chapter we will firstly present all previously obtained results on the topic of beam-induced dynamics in section 6.1. In the following sections all results obtained by our group during the beamtimes will be presented and interpreted. A more detailed discussion and an outlook on future experiments on the topic will be given in the next and final chapter.

6.1 Results of previous experiments

At the time this thesis was written, it was widely believed that X-rays to not change the structure of hard matter. And there have only been two studies on the possibility of beam-induced dynamics in solids. As mentioned in the introduction, the first study was done by Leitner et al. in 2015[4]. They investigated the effects of the beam on single-crystalline $Cu_{90}Au_{10}$ at PETRA III, Hamburg. The group studied the effect of X-rays on the dynamics of aforementioned material by measuring the same sample several times at temperatures of 543 K and 553 K respectively. Each measurement was carried out with different numbers of attenuators and therefore a different photon flux. They did not find any dependence of the correlation time τ on the photon flux. This indicates that the dynamics measured are internal and not beam-induced.

The second study was done by Ruta et al. in 2017[5]. Instead of a single crystal, they used vitreous silica (SiO_2) and vitreous germanium (GeO_2) for their experiments at ESRF, Grenoble. Both materials are oxide glasses. They also studied the effect of the beam on the dynamics by measuring every sample several times, each measurement with different numbers of attenuators. They conducted all measurements at room temperature, which is far below the glass transition temperature. At this temperature no measurable dynamics was expected. In contrast to this expectations they found a full decorrelation of the autocorrelation function, which means that there is measurable dynamics in the sample. Furthermore they found that the correlation time τ was inversely proportional to the flux F. This strongly indicates that the dynamics is not internal, but entirely beam-induced instead. In addition to this oxide glasses they also measured the dynamics in the metallic glass $Cu_{65}Zr_{27.5}Al_{7.5}$. In this material the group did not find any dependence of the dynamics on the photon flux.

From this previous works it can be concluded that different types of materials react differently to the beam, some of them showing beam-induced dynamics while others do not.

6.2 Experimental results

To get a better understanding of the nature and characteristics of this dynamics, our aim was to conduct an aXPCS measurement series with a broad range of different oxide glasses. An overview of all glasses prepared for the experiments is given in Tab. 4.1. However, due to technical difficulties not all measurements produced feasible results. Therefore not all samples listed in this table will be found in this chapter.

As in the previous works on the topic, we measured all samples several times using different numbers of attenuators. A single attenuator reduced the flux by a factor of e at ESRF and 2.07 at PETRA III. The number of attenuators used for a measurement ranged from zero attenuators up to three attenuators. A higher number was technically not possible, since every attenuator lowered the number of photons hitting the detector significantly and worsened the statistics. Since the total photon flux was unknown and different at both synchrotrons, comparing different samples with each other is only possible within the respecting synchrotron.

Furthermore, several samples were measured at different temperatures, ranging from room temperature (24 °C) to temperatures slightly above glass transition temperature T_g (see Tab. 4.1 for T_g of all samples). This was motivated by the assumption that slightly above T_g internal dynamics would be much more present compared to room temperature resulting in a weaker effect of the beam on the dynamics and a possibility to see internal dynamics.

6.2.1 Normalized autocorrelation functions

First and foremost we tested for every sample whether the dynamics measured were beam-induced or internal dynamics. For this purpose, the autocorrelation functions[1] that were acquired with different numbers of attenuators, but otherwise same conditions, were plotted together in one graph. This way they can be directly compared with each other.

Additionally, to only compare the functions by their physically interesting properties, i.e. τ and α, all autocorrelation functions were normalized with respect to the physically irrelevant parameters c_0 and β. Mathematically, the normalized ACF $g_n^{(2)}(\Delta t)$ takes the form

$$g_n^{(2)}(\Delta t) = (g^{(2)}(\Delta t) - c_0)/\beta \tag{6.1}$$

$$g_n^{(2)}(\Delta t) = e^{-2(\frac{\Delta t}{\tau})^{\alpha}} \tag{6.2}$$

In the case that the dynamics is entirely internal, all ACFs for a given sample must be the same. This implies that they overlap graphically within their margin of error. However, if the beam induces dynamics, the functions should behave differently and don't overlap.

The results for all samples are shown in Figures 6.1 to 6.14. The plots comparing the normalized ACFs are shown on the left side of each figure. The plots on the right side also show normalized intensity functions, but in addition to the normalization, the correlation time is rescaled with the relative flux of the beam. This is useful to check the other extreme case, where the dynamics is entirely beam-induced. In this case it is expected that the rescaled functions are the same within the margin of error.

[1] Autocorrelation functions for a specific sample that were measured under the exact same conditions, i.e. same photon flux, 2θ-angle and temperature were averaged. The average was weighted according to the number of frames recorded in a certain measurement.

Additionally to the plots, each figure contains information about the measurement settings (composition, temperature, 2θ-angle, synchrotron) and the physically relevant results, i.e. τ_i, the rescaled $\tau_i' = \tau_i \cdot F_i$ and α_i. It must be pointed out that there is only one α listed for each sample in contrast to τ. The α that is listed is the one that was measured for full flux, i.e. zero attenuators. With decreasing flux α get closer to one, which is non-physical and due to the worsening of the statistics.

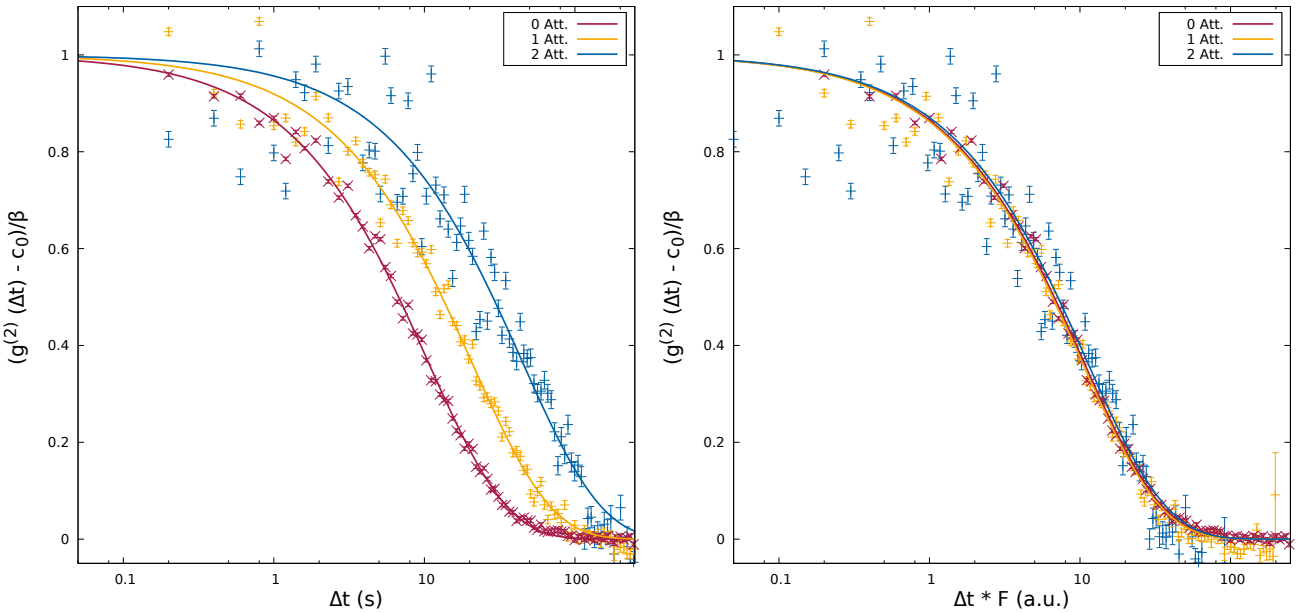

Figure 6.1: **Sample:** $(V_2O_5)_{50}(P_2O_5)_{50}$; T=24 °C; 2Θ=15°; measured at PETRA III, beamline P10; **Left:** Normalized intensity auto-correlation function. **Right:** Normalized intensity auto-correlation rescaled by the incoming relative flux.
Both sides: $\tau_0 = 24.21 \pm 0.31$ s, $\tau_1 = 46.30 \pm 0.92$ s, $\tau_2 = 97.42 \pm 3.95$ s
$\tau_1 \cdot F_1 = 22.37 \pm 0.44$ s, $\tau_2 \cdot F_2 = 22.74 \pm 0.92$ s; $\alpha = 0.82 \pm 0.02$

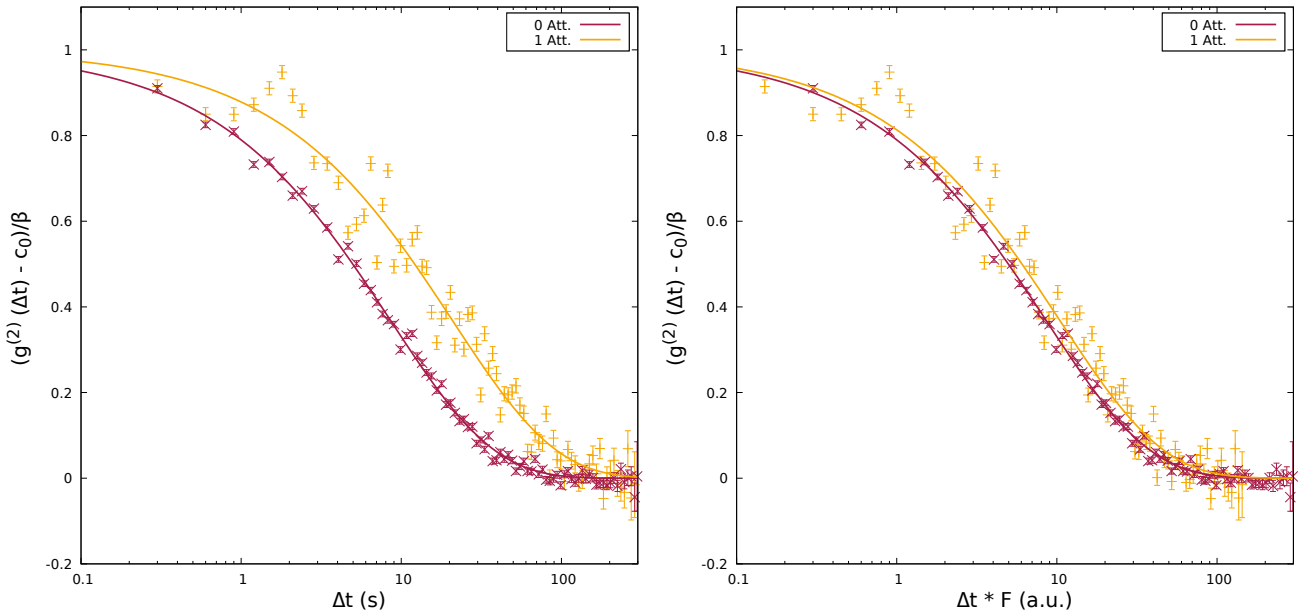

Figure 6.2: **Sample:** $(V_2O_5)_{75}(P_2O_5)_{25}$; T=24 °C; 2Θ=9°; measured at PETRA III, beamline P10; **Left:** Normalized intensity auto-correlation function. **Right:** Normalized intensity auto-correlation rescaled by the incoming relative flux.
Both sides: $\tau_0 = 24.08 \pm 0.59$ s, $\tau_1 = 58.63 \pm 2.92$ s
$\tau_1 \cdot F_1 = 28.32 \pm 1.44$ s, $\alpha = 0.67 \pm 0.01$

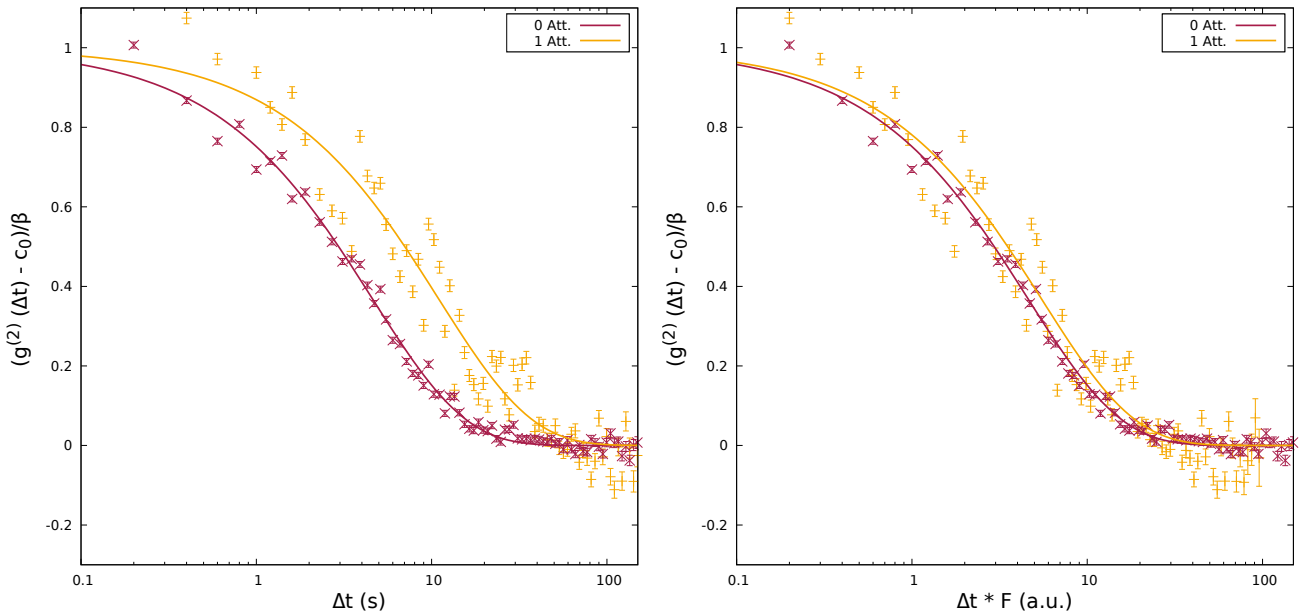

Figure 6.3: **Sample:** $(B_2O_3)_{100}$; T=24 °C; 2Θ=10°; measured at PETRA III, beamline P10; **Left:** Normalized intensity auto-correlation function. **Right:** Normalized intensity auto-correlation rescaled by the incoming relative flux.
Both sides: $\tau_0 = 10.70 \pm 0.40$ s, $\tau_1 = 25.71 \pm 2.64$ s
$\tau_1 \cdot F_1 = 12.42 \pm 1.28$ s; $\alpha = 0.82 \pm 0.05$

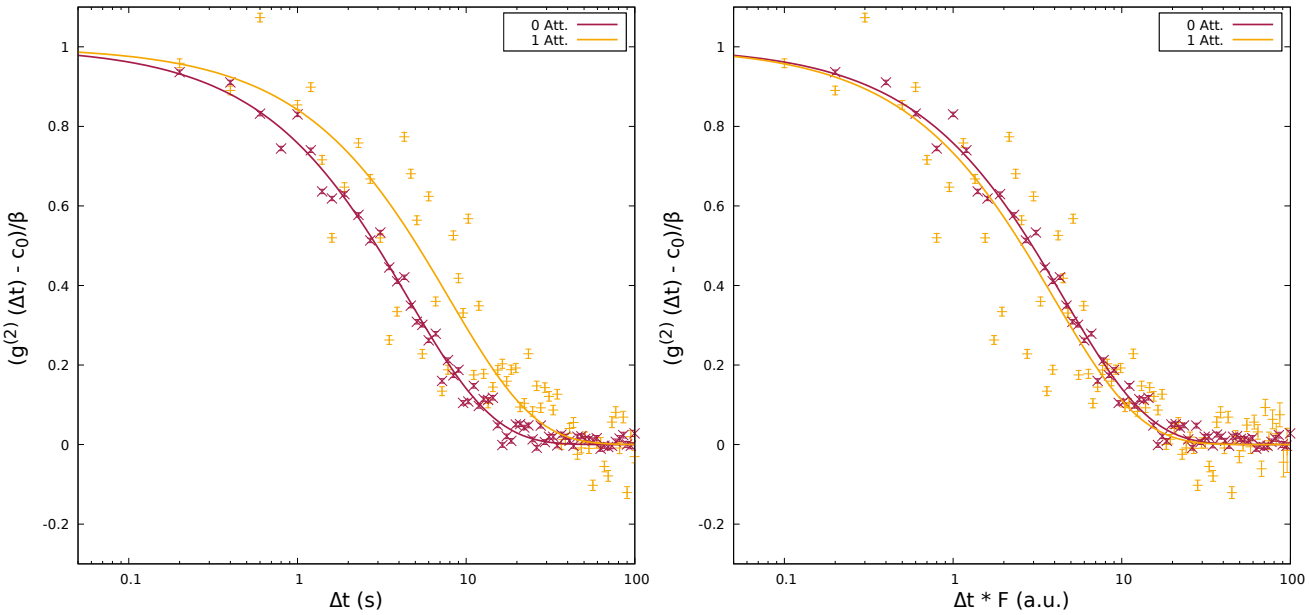

Figure 6.4: **Sample:** $(B_2O_3)_{100}$; T=24 °C; 2Θ=13°; measured at PETRA III, beamline P10; **Left:** Normalized intensity auto-correlation function. **Right:** Normalized intensity auto-correlation rescaled by the incoming relative flux.
Both sides: $\tau_0 = 9.83 \pm 0.35$ s, $\tau_1 = 23.99 \pm 2.69$ s
$\tau_1 \cdot F_1 = 11.59 \pm 1.30$ s; $\alpha = 0.85 \pm 0.05$

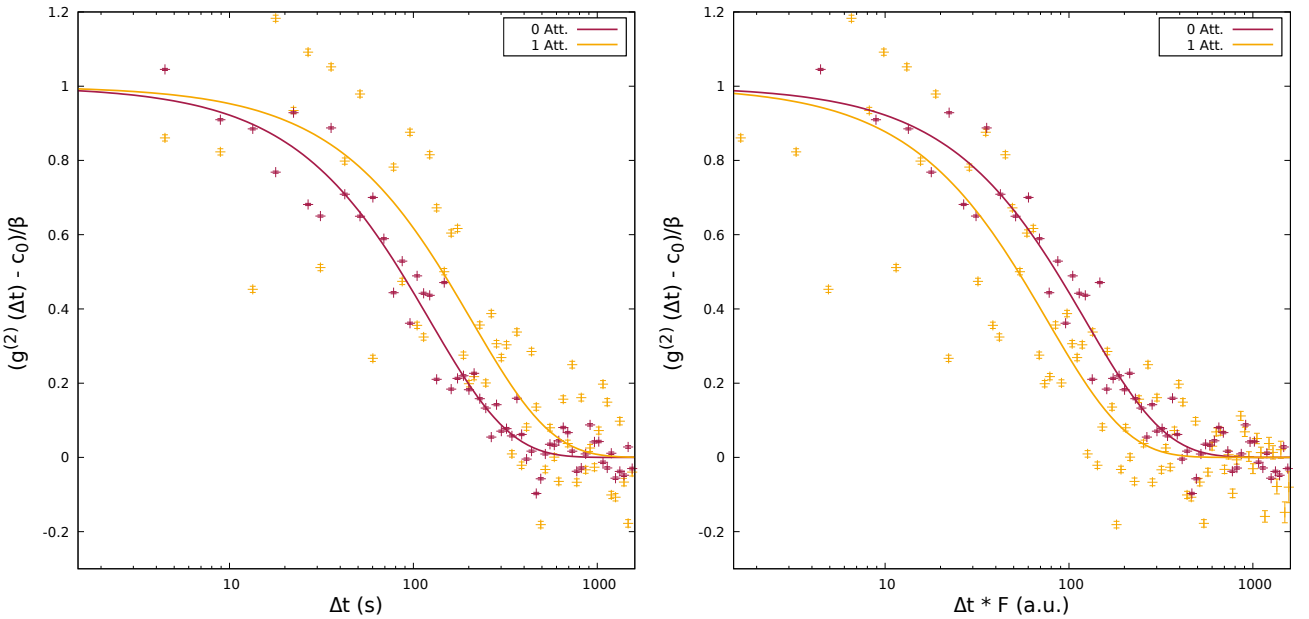

Figure 6.5: **Sample:** $(Li_2O)_{20}(B_2O_3)_{80}$; T=24 °C; 2Θ=10°; measured at ESRF, beamline ID10; **Left:** Normalized intensity auto-correlation function. **Right:** Normalized intensity auto-correlation rescaled by the incoming relative flux.
Both sides: $\tau_0 = 246.28 \pm 14.27$ s, $\tau_1 = 392.05 \pm 44.72$ s
$\tau_1 \cdot F_1 = 144.23 \pm 16.45$ s; $\alpha = 1.00 \pm 0.11$

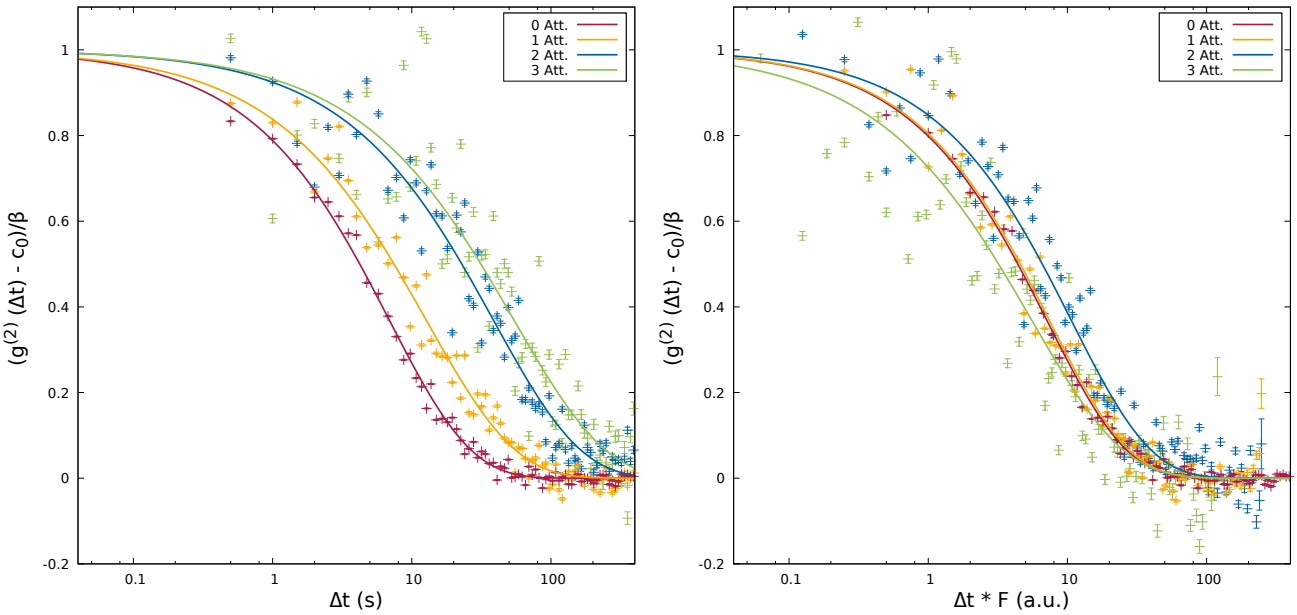

Figure 6.6: **Sample:** $(Na_2O)_5(B_2O_3)_{95}$; T=24 °C; 2Θ=14.5°; measured at PETRA III, beamline P10; **Left:** Normalized intensity auto-correlation function. **Right:** Normalized intensity auto-correlation rescaled by the incoming relative flux.
Both sides: $\tau_0 = 6.99 \pm 0.25$ s, $\tau_1 = 14.62 \pm 0.97$ s, $\tau_2 = 34.45 \pm 1.98$ s, $\tau_3 = 52.35 \pm 4.69$ s
$\tau_1 \cdot F_1 = 7.06 \pm 0.47$ s, $\tau_2 \cdot F_2 = 8.04 \pm 0.46$ s, $\tau_3 \cdot F_3 = 5.90 \pm 0.53$ s; $\alpha = 0.76 \pm 0.04$

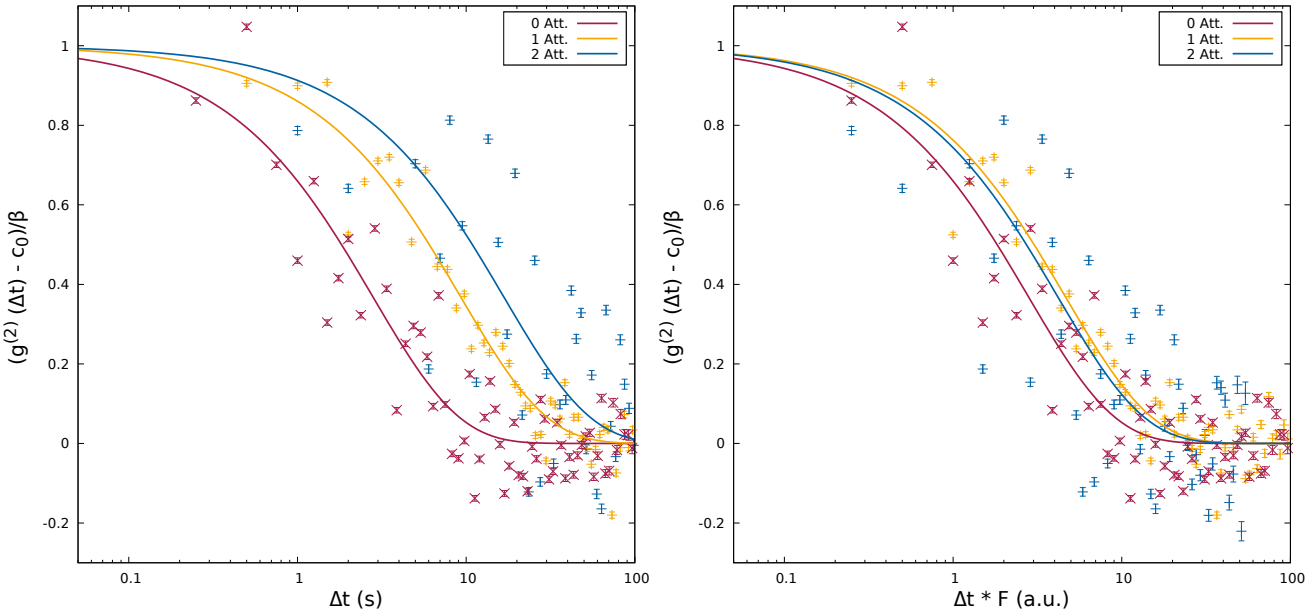

Figure 6.7: **Sample:** $(K_2O)_{20}(B_2O_3)_{80}$; T=24 °C; 2Θ=14.5°; measured at PETRA III, beamline P10; **Left:** Normalized intensity auto-correlation function. **Right:** Normalized intensity auto-correlation rescaled by the incoming relative flux.
Both sides: $\tau_0 = 6.30 \pm 1.18$ s, $\tau_1 = 19.75 \pm 1.99$ s, $\tau_2 = 30.01 \pm 7.37$ s
$\tau_1 \cdot F_1 = 9.54 \pm 0.96$ s, $\tau_2 \cdot F = 7.00 \pm 1.72$ s; $\alpha = 0.85 \pm 0.27$

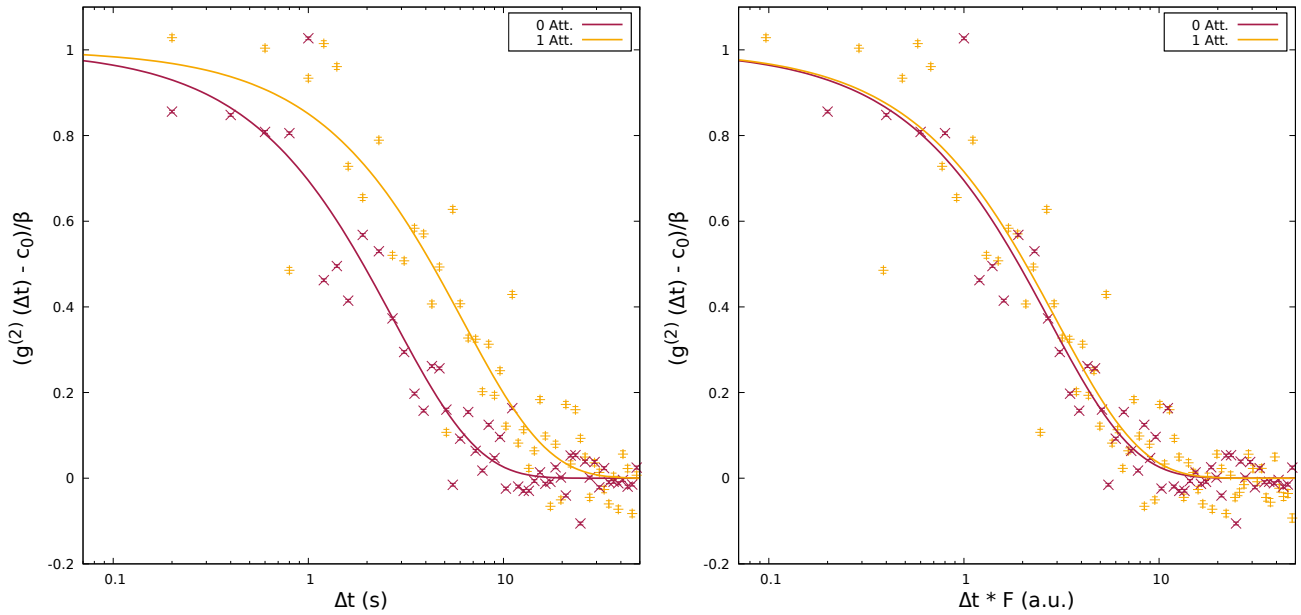

Figure 6.8: **Sample:** $(Rb_2O)_2(B_2O_3)_{98}$; T=24 °C; 2Θ=14°; measured at PETRA III, beamline P10; **Left:** Normalized intensity auto-correlation function. **Right:** Normalized intensity auto-correlation rescaled by the incoming relative flux.
Both sides: $\tau_0 = 5.51 \pm 0.42$ s, $\tau_1 = 12.35 \pm 0.88$ s
$\tau_1 \cdot F_1 = 5.97 \pm 0.43$ s; $\alpha = 1.00 \pm 0.15$

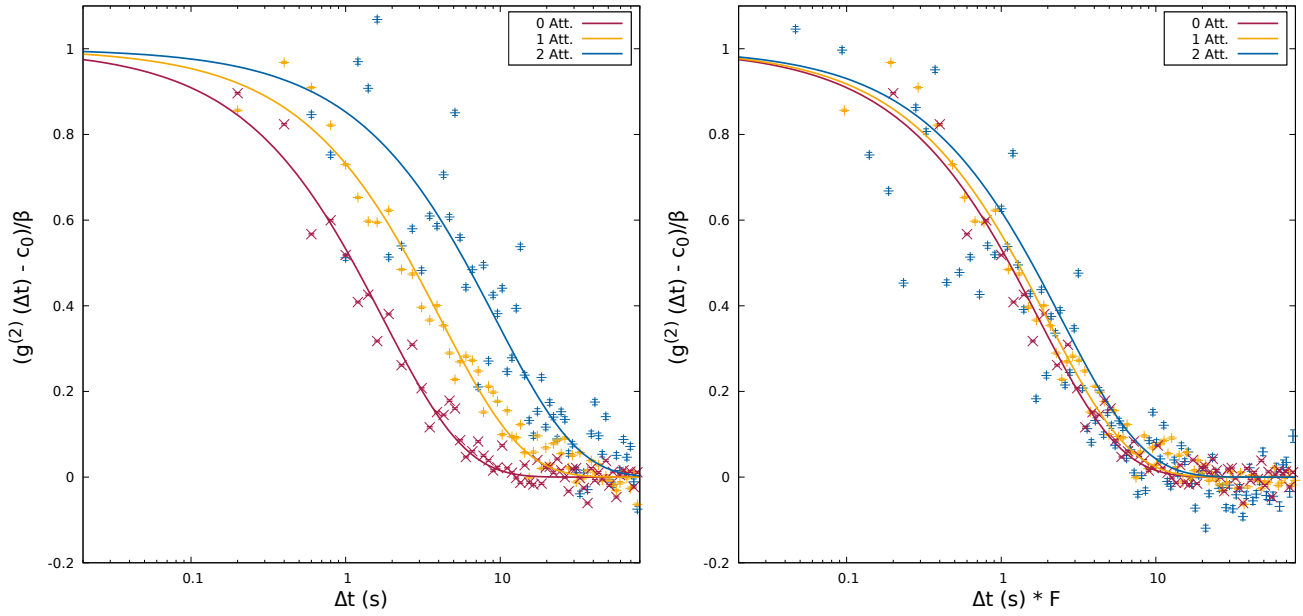

Figure 6.9: **Sample:** $(Rb_2O)_{15}(B_2O_3)_{85}$; T=24 °C; 2Θ=16°; measured at PETRA III, beamline P10; **Left:** Normalized intensity auto-correlation function. **Right:** Normalized intensity auto-correlation rescaled by the incoming relative flux.
Both sides: $\tau_0 = 3.35 \pm 0.34$ s, $\tau_1 = 7.79 \pm 0.56$ s, $\tau_2 = 19.01 \pm 1.57$ s
$\tau_1 \cdot F_1 = 3.76 \pm 0.27$, $\tau_2 \cdot F_2 = 4.44 \pm 0.37$; $\alpha = 0.82 \pm 0.13$

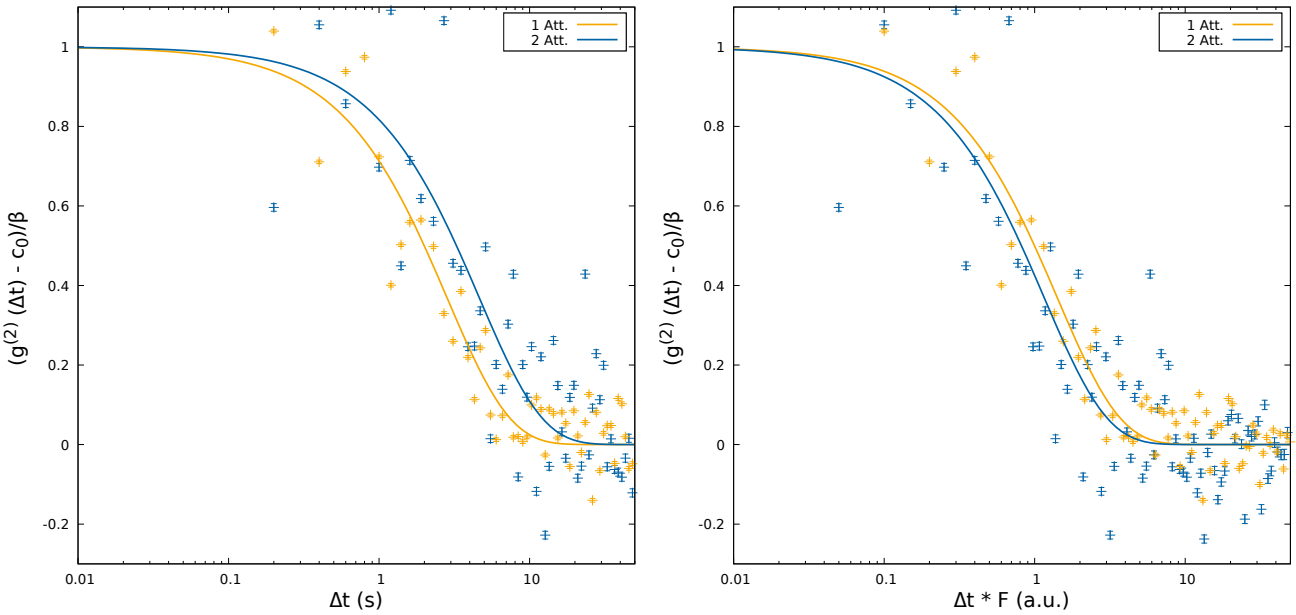

Figure 6.10: **Sample:** $(Cs_2O)_2(B_2O_3)_{98}$; T=24 °C; 2Θ=10°; measured at PETRA III, beamline P10; **Left:** Normalized intensity auto-correlation function. **Right:** Normalized intensity auto-correlation rescaled by the incoming relative flux.
Both sides: $\tau_1 = 4.76 \pm 0.62$ s, $\tau_2 = 7.21 \pm 1.72$ s
$\tau_1 \cdot F_1 = 2.30 \pm 0.30$ s, $\tau_2 \cdot F_2 = 1.68 \pm 0.40$ s; $\alpha = 1.04 \pm 0.28$

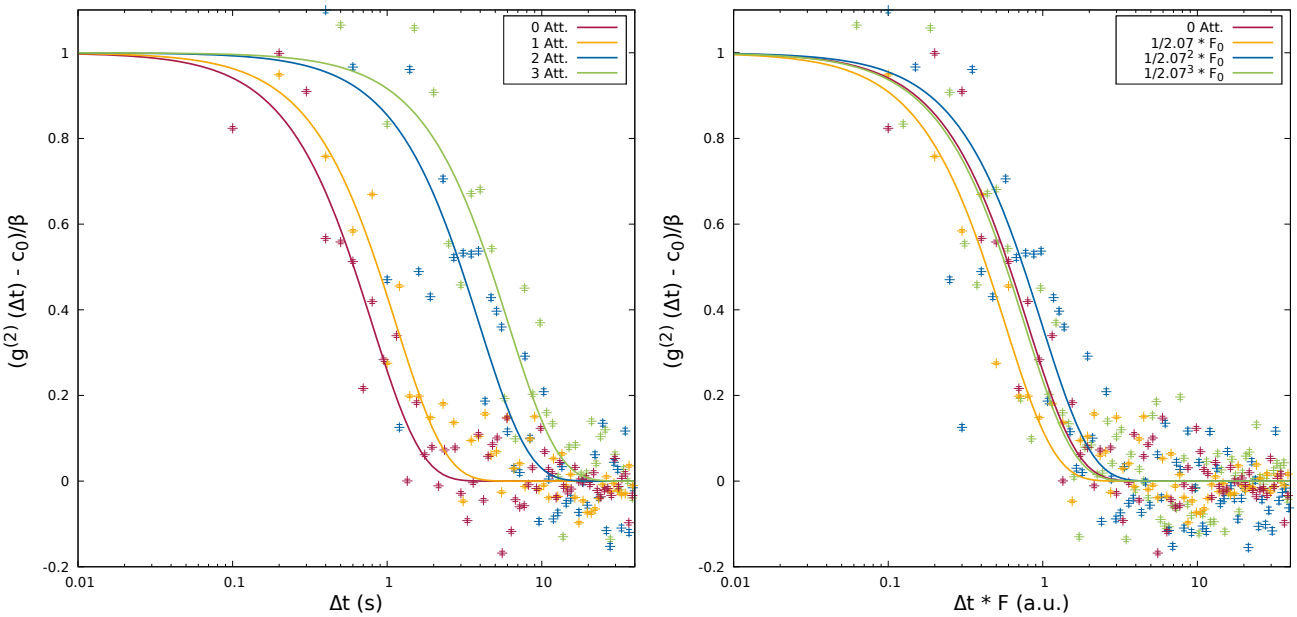

Figure 6.11: **Sample:** $(Cs_2O)_{15}(B_2O_3)_{85}$; T=24 °C; 2Θ=15°; measured at PETRA III, beamline P10; **Left:** Normalized intensity auto-correlation function. **Right:** Normalized intensity auto-correlation rescaled by the incoming relative flux.
Both sides: $\tau_0 = 1.33 \pm 0.18$ s, $\tau_1 = 1.92 \pm 0.23$ s, $\tau_2 = 6.21 \pm 1.09$ s, $\tau_3 = 9.62 \pm 1.70$ s
$\tau_1 \cdot F_1 = 0.93 \pm 0.11$ s, $\tau_2 \cdot F_2 = 1.45 \pm 0.25$ s, $\tau_3 \cdot F_3 = 1.08 \pm 0.19$ s; $\alpha = 1.35 \pm 0.46$

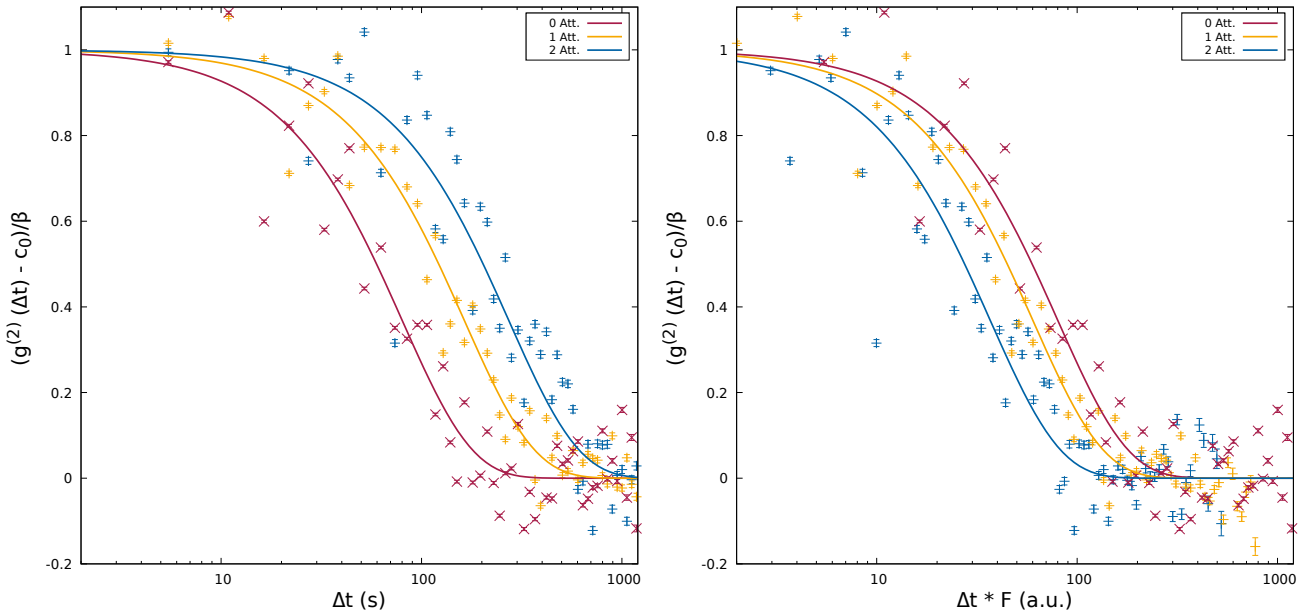

Figure 6.12: **Sample:** $(Rb_2O)_{15}(SiO_2)_{85}$; T=460 °C; 2Θ=25°; measured at ESRF, beamline ID10; **Left:** Normalized intensity auto-correlation function. **Right:** Normalized intensity auto-correlation rescaled by the incoming relative flux.
Both sides: $\tau_0 = 146.35 \pm 14.86$ s, $\tau_1 = 295.07 \pm 22.76$ s, $\tau_2 = 534.69 \pm 64.10$ s
$\tau_1 \cdot F_1 = 108.55 \pm 8.37$ s, $\tau_2 \cdot F_2 = 72.37 \pm 8.67$ s; $\alpha = 1.24 \pm 0.25$

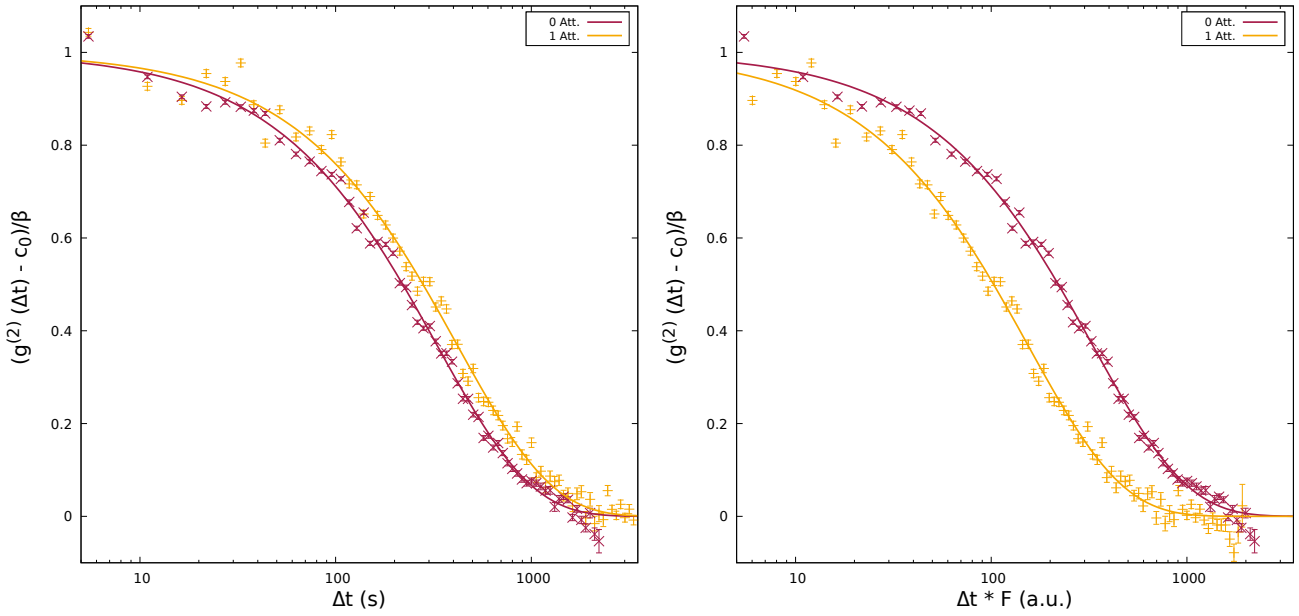

Figure 6.13: **Sample:** $(PbO)_{30}(SiO_2)_{70}$; T=490 °C; 2Θ=20°; measured at ESRF, beamline ID10; **Left:** Normalized intensity auto-correlation function. **Right:** Normalized intensity auto-correlation rescaled by the incoming relative flux.
Both sides: $\tau_0 = 711.56 \pm 24.95$ s, $\tau_1 = 892.49 \pm 40.46$ s
$\tau_1 \cdot F_1 = 328.33 \pm 14.88$ s; $\alpha = 0.90 \pm 0.04$

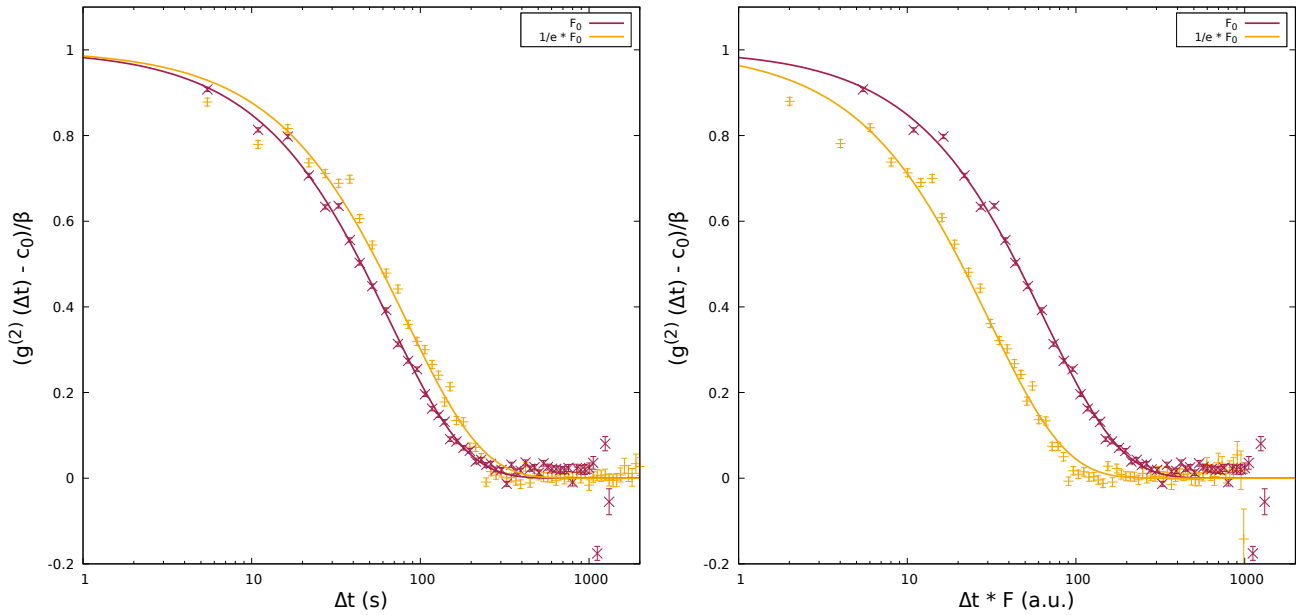

Figure 6.14: **Sample:** $(PbO)_{30}(SiO_2)_{70}$; T=510 °C; 2Θ=20°; measured at ESRF, beamline ID10; **Left:** Normalized intensity auto-correlation function. **Right:** Normalized intensity auto-correlation rescaled by the incoming relative flux.
Both sides: $\tau_0 = 134.39 \pm 10.01$ s, $\tau_1 = 171.37 \pm 3.66$ s
$\tau_1 \cdot F_1 = 63.04 \pm 1.34$ s; $\alpha = 0.96 \pm 0.14$

All figures show that the autocorrelation functions on the left side are distinct from each other and don't overlap. This can also be seen when looking at the τ's, since all of them are different within the margin of error. This confirms the results obtained by Ruta et al. that there is in fact beam-induced dynamics in oxide glasses. Furthermore it extends the previous knowledge by showing that borate glasses and phosphate glasses also show beam-induced dynamics, not only silicate and germanium glasses.

Now that we know that the dynamics depend on the beam, it raises the question whether the dynamics is entirely beam-induced or a mixture of internal and beam-induced dynamics. This question can be answered with the help of the rescaled autocorrelation functions on the right side of above figures. They allow us to group the results together in three categories:

First category: Entirely beam-induced dynamics

The first category consists of the samples in Figures 6.1 to 6.4 and Figures 6.6 to 6.11. In this category, the rescaled ACFs for the respective glasses overlap or are very close to overlapping. Therefore the rescaled τ's are they same within the margin of error or almost the same for the respective sample. This means that the dynamics is inversely proportional to the photon flux or very close to it, which implies that the dynamics is entirely beam-induced.

As mentioned above some samples to not entirely overlap within their respective margin of error. The deviations seem random and small. We therefore expect that this is due to imprecisions in our measurements. However, a physical reason cannot be ruled out entirely.

All samples in this category were measured at room temperature, which is quite far beneath glass transition temperature T_g. $(V_2O_5)_{75}(P_2O_5)_{25}$ (Fig. 6.2) has the lowest T_g with a value of $T_g = 275.9$ °C, giving a difference between T_g and room temperature of $\Delta T = 251.9$ °C. This far

beneath glass transition no internal dynamics is expected, which is in agreement with our results.

Second category: Mixture of beam-induced and internal dynamics

The second category consists of the samples in Figures 6.12 to 6.14. For the samples in this category, the rescaled ACFs to not overlap, they show a different behaviour. This can best be understood by looking at the τ's. After rescaling with the flux, the τ's from the measurements with a higher number of attenuators become smaller than the τ's with a lower number of attenuators. This behaviour shows that the dynamics here is not inversely proportional to the flux. Instead the influence of the beam on the dynamics is less strong compared to the samples in the first category. This indicates that the measured dynamics is a mixture between internal and beam-induced dynamics.

The samples in this category were measured far above room temperature and also slightly above T_g. The difference between T_g and the measurement temperature T was 4.1 K for the sample 6.12, 10.1 K for 6.13 and 30.1 K for 6.14. At this temperatures internal dynamics was expected and our results seem to be in agreement with this expectations.

However, there is also the possibility that this dynamics was relaxation dynamics due to the increase of temperature. Dynamics of this kind will be discussed in section 6.2.3. Although theoretically possible it is unlikely, since relaxation dynamics caused by an increase in temperature is characterised by a large α, which is around 2. The measurements in this category have an α around 1. This is a strong indicator for equilibrium dynamics.

Third category: Ambiguous results

The third category consists only of sample Fig. 6.5. This $(Li_2O)_{20}(B_2O_3)_{80}$ sample shows a beam-dependence similar to the samples in the second category. This is quite surprising, since this sample was measured at room temperature. This is far beneath glass transition temperature and no other glass composition showed internal dynamics at room temperature. However, lithium is the lightest alkali metal after all and the the atoms should be more free to move than atoms of other alkali metals. The other possible cause for this results is a systematic error during measurement.

To decide whether the measured dynamics is (partially) internal or a systematic error occurred, further measurements will be necessary.

6.2.2 Properties of beam-induced dynamics

We now know that all oxide glasses investigated show beam-induced dynamics. However, this raises several follow-up question concerning the concrete mechanism of the dynamics. The ones that will be addressed here are the following:

1. Is the dynamics depending on the the total dose of radiation or is the dynamics stationary?
2. How fast do the dynamics follow the flux of the beam when it is changed?
3. Are the beam irradiation effects changing the glass structure permanently?

To answer this questions a measurement series was conducted at ESRF for a $(PbO)_{30}(SiO_2)_{70}$ sample at 510 °C. During this measurement an attenuator was switched in and out several times. With the long time of the measurement we were able to study the effects of the total dose on the dynamics. And with the switching of the attenuator we were able to study how the dynamics adjust to the change of the flux.

It must be mentioned that a temperature of 510 °C was not ideal here, since this glass already shows internal dynamics at this temperature. However, the internal dynamics does not depend on the flux and therefore stay constant during the measurement. This means that we should still be able to answer the questions posed above.

The results of the measurement are shown in Fig. 6.15 and in Tab. 6.1.

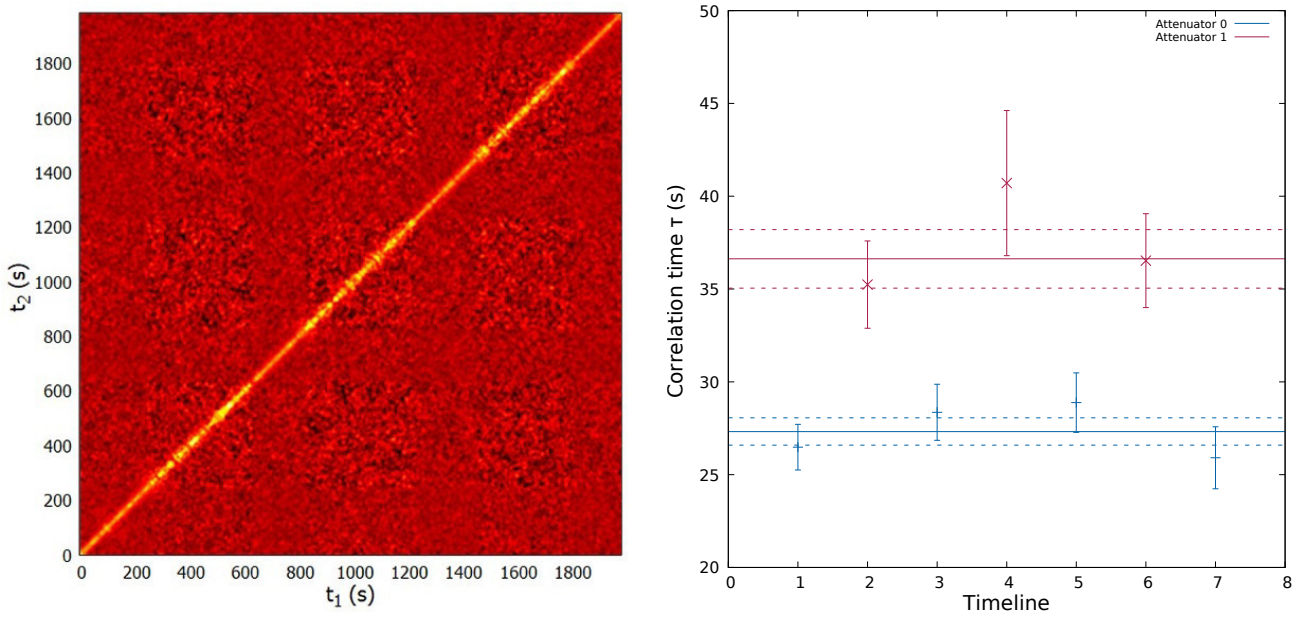

Figure 6.15: **Left:** Two-times correlation function. The time arrow goes from the lower left to the upper right corner. The measurement starts without attenuator and also ends without attenuator. **Right:** The plot shows τ as a function of the time step. Time step here means a section with constant flux. For example, the first time step goes from the beginning of the measurement to the insertion of the first attenuator. For the actual time data (in seconds) see Tab. 6.1. The continuous lines are the weighted mean values for the respective measurement series. The dashed lines are mean values plus/minus the weighted error of the respective series.

Nr.	Attenuator	τ (s)	$\Delta\tau$ (s)	α	$\Delta\alpha$	# Frames	Frame-time (s)
1	0	26.48	1.23	1.15	0.11	247	5.4577
2	1	35.24	2.35	1.23	0.17	384	5.4577
3	0	28.36	1.51	1.26	0.14	198	5.4577
4	1	40.71	3.91	1.35	0.23	403	5.4577
5	0	28.88	1.60	0.96	0.10	223	5.4577
6	1	36.53	2.53	1.29	0.19	353	5.4577
7	0	25.91	1.67	1.12	0.14	178	5.4577

Table 6.1: Detailed information about the conducted measurement. The first column corresponds to the x-axis in the plot on the right side of Fig. 6.15. To calculate the actual time (in seconds) of each time step, the number of frames must be multiplied with the frame-time.

With the results of this measurement, it is possible to answer the three questions addressed above:

1. In the two-times correlation function above, sections with the same number of attenuator (either 0 or 1) appear to be similar. This is also reflected in the τ's. They are the same within their margins of error for a given flux. Furthermore, the two-times correlation function only changes when the attenuator is switched in and out. There is no broadening or narrowing within a given section. This observations imply that the dynamics is only depending on the current photon flux. Hence, they are independent of the cumulated dose.

2. When the attenuator is switched in or out, the two-times correlation function changes. The change in dynamics must be a very fast process, since the two-times correlation functions is constant within a given section. The upper time-limit of adjustment of the dynamics must therefore be smaller than the time per frame, which is 5.4577 s.

3. The third question cannot be fully answered with this measurement. To see whether and how the structure of the glass changes under the radiation, an X-ray diffraction experiment that measures the intensity as a function of the wave vector q, i.e. $I(q)$, would be necessary before and after the sample is exposed to the beam.

   However, the measurement strongly indicates that there is no permanent structural change in the glass. In the case of structural changes one would expect a broadening in the two-times correlation function. This broadening is expected due to the fact that diffusion is faster during the structural change and slows down after the structure has changed. We did not observe any broadening of the two-times correlation function in any sector. This indicates that for the time of the measurement no structural change occurred.

6.2.3 Temperature-alteration induced relaxation dynamics

As stated above, we did not only measure samples at room temperature, but also at higher temperatures. The standard procedure to do this type of measurement was to heat up the sample, adjust all necessary parameters at the beamline and then start the measurement.

The main sample for this series of measurements was $(PbO)_{30}(SiO_2)_{70}$. Firstly, the sample was measured several times at room temperature. After this measurement series the temperature was raised to 460 °C, where the same kind of measurement series was performed. This procedure was repeated with 490 °C and 510 °C. In detail, the sample was held at 460 °C for about 1262 min until heating up to 490 °C. At this temperature, the sample was held for about 1945 min and then heated up to the maximal temperature of 510 °C. Between the main measurement series some small measurements and minor temperature alterations were performed.

At the time of this measurements beam-induced dynamics was already known. Therefore we expected to measure different τ's for different numbers of attenuators, but the same τ (within the margin of error) for the same number of attenuator, i.e. the same photon flux. However, the actual results of the measurements were quite different from this expectations, as can be seen in Fig. 6.16, 6.17 and 6.18. All figures show that τ increases with time, meaning that the dynamics in the sample is slowing down.

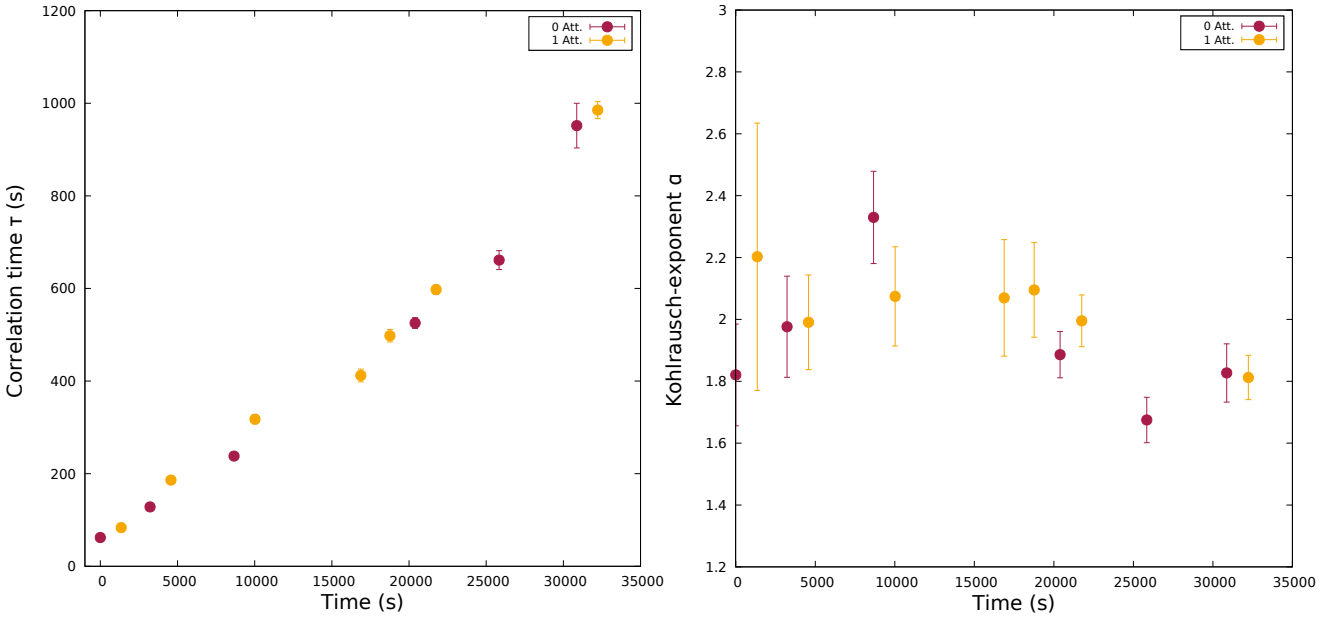

Figure 6.16: **Sample:** $(PbO)_{30}(SiO_2)_{70}$; $T_0 = 460$ °C; $\Delta T^2 = 436$ K
Time between reaching temperature T_0 and first measurement: 68 min
Left: Correlation time τ as a function of time **Right:** Kohlrausch exponent α as a function of time

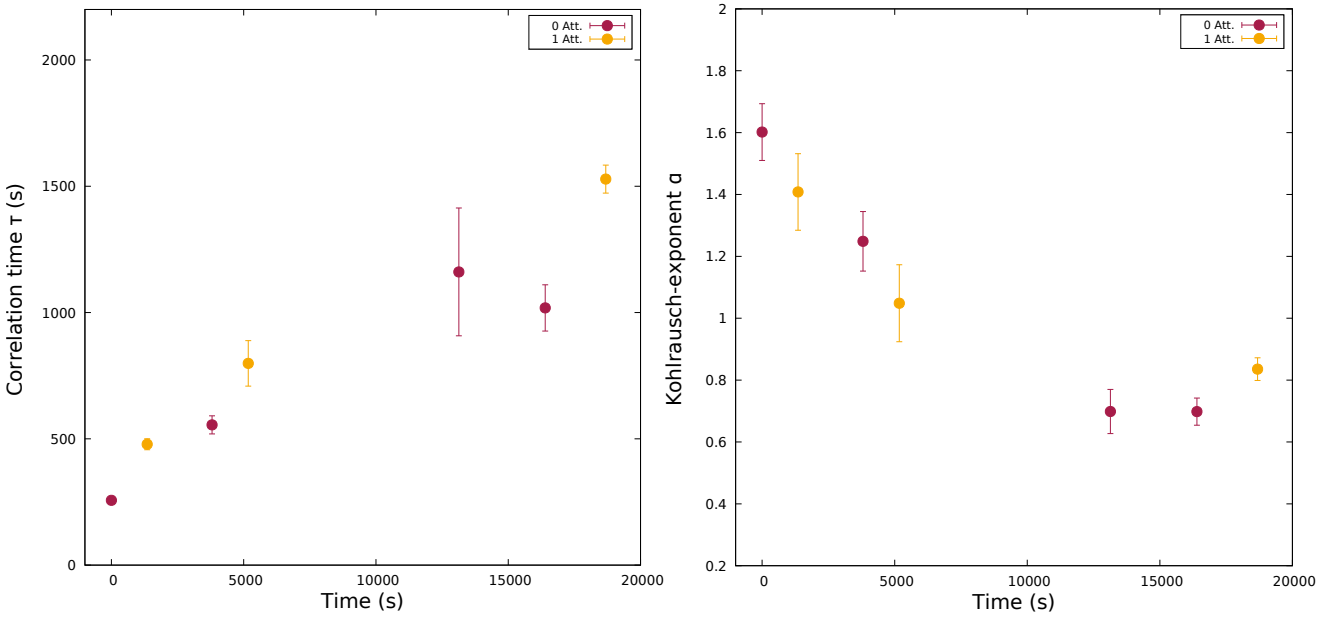

Figure 6.17: **Sample:** $(PbO)_{30}(SiO_2)_{70}$; $T_0 = 490$ °C; ΔT: 30 K
Time between reaching temperature T_0 and first measurement: 59 min
Left: Correlation time τ as a function of time **Right:** Kohlrausch exponent α as a function of time

[2] ΔT refers to the difference of the temperature before heating up and the actual temperature T_0 during the respective measurement series.

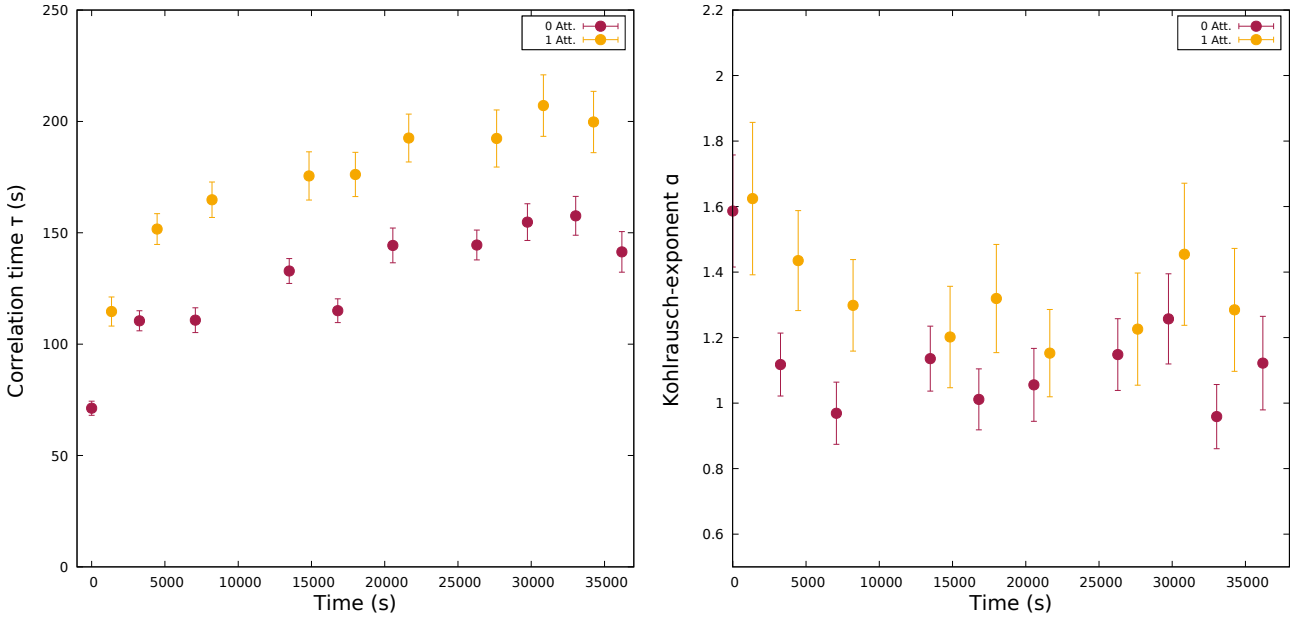

Figure 6.18: **Sample:** $(PbO)_{30}(SiO_2)_{70}$; $T_0 = 510$ °C; ΔT: 20 K
Time between reaching temperature T_0 and first measurement: 22 min
Left: Correlation time τ as a function of time **Right:** Kohlrausch exponent α as a function of time

This behaviour is different from the beam-induced dynamics investigated in the previous sections. It can also not be explained by regular internal dynamics, since this dynamics is slowing down very fast, as can be seen in the fast increase of τ. It can best be explained by the assumption that these are relaxation dynamics caused by the increase in temperature. This dynamics occurs due to the amorphous nature of glass. When the temperature is changed the complex potential energy landscape changes as well and the atoms rearrange into a new metastable state.

The change in the τ's is most extreme in Fig. 6.16. This can be explained by the fact that the difference of temperature was the highest for this measurement series. The sample was heated up from room temperature, making a change in temperature of 436 K. When we conducted the series of measurements the sample was still in the middle of the relaxation process. This can also be seen in the values of the Kohlrausch-exponent α. It is at a value of around $\alpha = 2$ for all measurements. This is significantly higher than for glasses that were measured in a frozen metastable state, where the value of α was around 1 or less.

In Fig. 6.17 there is also a change in the τ's, but with the difference that at the end of the measurement series the change in τ becomes smaller. This behaviour is in accordance with the α's. They are clearly above 1 at first, but fall rapidly to values around 1 or less at the end of the measurement series, which is a sign that the glass sample reaches an equilibrium state. The reason why the relaxation here seems to be faster than the relaxation at 460 °C is probably the fact that the change in temperature was 30 K and therefore far less than the change from room temperature to 460 °C. Also the temperature here is already 10.1 K above glass transition temperature, which means that dynamics is faster in general and this might be the reason for faster relaxation dynamics as well.

Finally, a third measurement series was conducted at 510 °C. The results can be seen in Fig. 6.17. Here it can be seen that the relaxation process happens very fast. Only the first couple of τ's are smaller than the rest. After around 10,000 seconds all tau's are the same within their margin of

errors and their respective number of attenuators. This is also in accordance with the behaviour of α. It decreases slightly in the beginning and then stays constant. This behaviour of the τ's and the α's is logically consistent with what we have seen at 460 °C and at 490 °C. Here, the temperature change was 20 K, which is less than before and the temperature is 30.1 K above glass transition temperature. Therefore, it is expectable that the relaxation process is fast. This is in agreement with our data.

6.3 Summary

First and foremost, the aim of this thesis was to answer the question, whether there exist beam-induced dynamics in samples. This question can be answered with a clear yes. There is beam-induced dynamics in all samples investigated. Moreover, several questions of detail concerning the properties of the dynamics could have been resolved. The main results can be summarized as following:

- At room temperature the dynamics of all samples is proportional to the beam flux, except for one sample. After rescaling with the relative flux, the ACFs for a certain sample overlap. This clearly indicates that all dynamics measured is beam-induced and no internal dynamics is present.

  The one exception here is the sample containing lithium. Lithium is the lightest alkali metal and moves more freely than other alkali metals. Internal dynamics at room temperature is possible for this element. However, a systematic error can't be ruled out and further measurements are necessary to come to a definite answer.

- At temperatures slightly above glass transition temperatures the ACFs are not proportional to the flux. This is because the influence of the beam is weaker than at room temperature. This strongly implies that the observed dynamics is a mixture between beam-induced and internal dynamics.

- The beam induced dynamics has the following properties:

  It is independent of the accumulated dose and only depend on the current flux. It also adapts very fast to a change in the flux. The upper limit for the adaptation is 5.477 s, which corresponds to the time it took to record one frame. However this is only an upper limit, the actual adjustment is probably much faster.

- Beside beam-induced and internal dynamics a third type has been observed. This dynamics occurs during structural relaxation caused by a change in temperature. One can call this third type an order-order relaxation in analogy to the analogue process known from intermetallic compounds.

Chapter 7

Discussion and outlook

We can now say with great certainty that there is beam-induced dynamics occurring in oxide glasses. First of all, this is a quite surprising result considering the fact, that it was believed for a long time that hard matter is unaffected by X-rays. It is not only surprising, but from today's perspective this effect is unwanted. This is obvious considering the fact, that the idea behind aXPCS is to have a technique that is capable of measuring internal dynamics in solids. In theory, this is a great advantage compared to techniques such as quasi-elastic neutron scattering or Mößbauer spectroscopy, since they can only be applied to a limited number of isotopes. In this chapter the separation of internal and beam-induced dynamics will be discussed as well as the possibility of measuring relaxation dynamics. Furthermore, some possible mechanisms underlying beam-induced dynamics will be debated. Finally, an outlook on future experiments will be given.

7.1 Separation of internal and induced dynamics

The biggest issue is whether the internal dynamics can be separated from the beam-induced dynamics. It is known that diffusion in solid state matter can be well described by the Arrhenius equation

$$D = D_\infty \cdot e^{-E_A/k_B \cdot T}, \tag{7.1}$$

where D_∞ is the Diffusion coefficient at infinite temperature, E_A is the activation energy, T is the absolute temperature and k_B is Boltzmann's constant. We have seen so far that at temperatures where there is only beam-induced dynamics, the dynamics is proportional to the flux Φ. In the case that the beam-induced dynamics depends on the flux, but is independent of the temperature, the Arrhenius equation could be modified in the following way:

$$D = D_\infty \cdot e^{-E_A/k_B \cdot T} + D_{\mathsf{beam}}(\Phi) \tag{7.2}$$

Here, $D_{\mathsf{beam}}(\Phi)$ is the contribution due to beam-induced dynamics. This diffusion term is a function of the flux, as we have seen. The situation becomes more complicated, if the beam-induced dynamics depends on the temperature T as well. Then we have the following Arrhenius equation:

$$D = D_\infty \cdot e^{-E_A/k_B \cdot T} + D_{\mathsf{beam}}(\Phi, T) \tag{7.3}$$

In this case, $D_{\text{beam}}(\Phi, T)$ also depends on the temperature of the setup. To test this experimentally, one must measure the diffusion coefficient for different temperatures. The temperatures must be low enough so that there is no internal diffusion occurring. Then a functional form of $D_{\text{beam}}(\Phi, T)$ could be gained. However, a possible dependence on the temperature has not been tested in the course of this thesis, therefore no definite answer can be given on whether the beam-induced dynamics is temperature-dependent or not.

7.2 Mechanism of beam-induced dynamics

There is one important aspect to the issue that has not been discussed yet, which is the mechanism behind beam-induced dynamics. In this section we will discuss on how the sample possibly absorbs the energy, how it affects the sample and where the energy goes. There have been several ideas proposed in the past, of whom the most important ones will be mentioned here.

7.2.1 Macroscopic heating

Internal diffusion is a thermally activated process. This means that diffusion will be faster when the temperature is raised. We have seen in the previous chapter that beam-induced dynamics shows a similar behaviour, the stronger the flux the faster the diffusion. This suggests to treat the beam as a source of heat, Hence, we calculated how much the sample gets heated by the beam. The geometry for this is shown in Fig. 7.1.

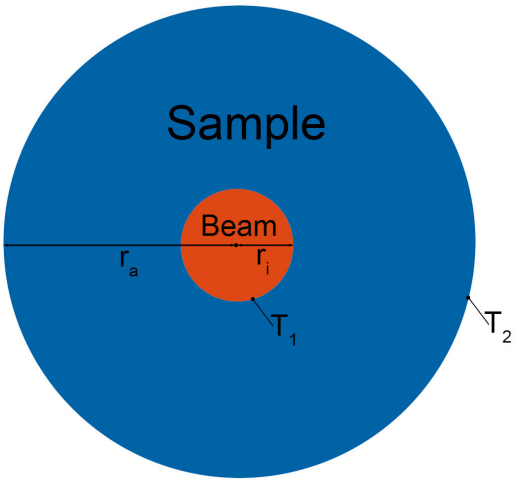

Figure 7.1: Two-dimensional illustration of macroscopic heating. Ideally, the beam hits the sample in the middle and the photon flux is perpendicular to the sample. The sample is of circular shape and surrounded by the sample holder.

The difference in temperature $\Delta T = T_1 - T_2$ between the edge of the illuminated area and the sample holder is given by Fourier's law

$$\Delta T = \frac{\dot{Q}}{\lambda \cdot F}, \tag{7.4}$$

where $\dot{Q}$ is the heating power of the beam, λ is the thermal conductivity of the sample and F is a geometrical factor. Mathematically, above equation is a steady-state solution to the two-dimensional heat conduction equation. The sample holder on the edge of the sample acts as a heat sink, therefore T_2 is at a fixed value. The analytical form of the geometrical factor for the given geometry is[1]

$$F = \frac{2 \cdot \pi \cdot L}{ln(\frac{r_a}{r_i})}. \tag{7.5}$$

L is the thickness of the sample, r_i is the radius of the beam and r_a is the radius of the sample, i.e. the distance from the middle of the sample to the sample holder. The temperature in the beam irradiated area is then $T_1 = T_2 + \Delta T$.

An explicit calculation was done by Leitner et al.[4]. They calculated the heating of a copper-containing alloy (90 at.% Cu and 10 at.% Au) for a typical aXPCS setup. They assumed a continuous beam with a flux of $2 \cdot 10^{11}$ photons per second, a photon energy of 8 keV and a beam diameter of 5 μm. The sample in the example was a 10 μm thin foil. The alloy had a heat conductivity of λ = 380 W/(m·K). In transmission geometry and under the assumption that half of the photons get absorbed the beam has a heating power of 0.13 mW. Heat radiation is neglected in this calculation. Applying Eq. (7.4) gives a difference in temperature of ΔK = 0.036 K between the edge of the illuminated area and the sample holder.

Here, a similar calculation was done for vitreous silica[2]. We adopted all parameters from above calculation. The only two differences were the thickness L = 50 μm of the sample and the heat conductivity, which for vitreous silica is 1.37 W/(m·K) at 25 °C[29]. Then Eq. (7.4) gives a difference in temperature of ΔT = 2.02 K. This is much higher than the value for the Cu alloy, but still very small and can therefore be neglected.

7.2.2 Primary knock-on atomic displacement

Since a macroscopic view is not sufficient to explain beam-induced dynamics, a microscopic view on the situation is needed. It is known that gamma rays cause radiation damage through knock-on displacements. A primary knock-on displacement[30] is defined as the displacement of a whole atom by collision with incident particles. This is in contrast to the displacement of an electron, which is called ionization. The mechanism of ionization will be described in section 7.2.3. The incident particles here are photons. The process behind the scattering of particles under incoming photons is called Compton scattering. Mathematically, the Compton scattering formula is given by

$$\lambda' = \lambda + \frac{h}{m \cdot c}(1 - cos\theta), \tag{7.6}$$

where λ and λ' are the wavelengths before and after scattering, h is Planckś constant, c the speed of light, m the mass of the target particle and θ is the scattering angle. Above equation can be rewritten in terms of the energy shift instead of the shift in wavelength:

$$E' = \frac{m \cdot c^2 \cdot E}{m \cdot c^2 + E \cdot (1 - cos\theta)}, \tag{7.7}$$

[1] The geometrical factor was obtained from *http://www.itw.uni-stuttgart.de/dokumente/Lehre/waermeuebertragung/2_Waermeleitung.pdf* (January 23, 2018)

[2] Vitreous silica was chosen because the thermal conductivity λ is very well know for this material. The argumentation holds for other oxide glass compositions as well, since they all have quite similar values for λ.

where E and E' are the energy before and after scattering. The difference in wavelength and energy respectively becomes maximal for a scattering angle of $\theta = 180°$:

$$\lambda' = \lambda + \frac{2 \cdot h}{m \cdot c} \tag{7.8}$$

$$E' = \frac{m \cdot c^2 \cdot E}{m \cdot c^2 + 2 \cdot E} \tag{7.9}$$

Eq. (7.8) shows that the difference in wavelength is a function of the mass m of the target. The heavier the target is the smaller the difference in the wavelength before and after scattering. This implies that heavy particles can absorb less energy from a photon than light particles. The lightest element used in this thesis is lithium. According to Eq. (7.8), a lithium nucleus can absorb a maximal energy of 0.019 eV from an 8 keV photon. However, in order to break atomic bonds by this mechanism energy transfer of at least several eVs would be necessary.

Furthermore, the cross section [3] for Compton scattering of photons and nuclei is very small. This means that it is very unlikely that a photons scatters at a nucleus. Even when it does, the energy transfer is to small to displace the nucleus. Hence, knock-on displacements can be ruled out as well as a possible mechanism behind beam-induced dynamics.

7.2.3 Ionization of atoms

Both, macroscopic heating as well as primary knock-on displacements of atoms due to Compton scattering can't explain beam-induced dynamics sufficiently. The first mechanism fails as an explanation due to the fact that the heating does not raise the temperature enough to cause such strong diffusion as seen in all glasses. The second mechanism introduced, Compton scattering of the photons with the nucleus, does not provide enough energy to kick atoms directly out of their position in the network and has a negligible cross section.

It is more likely that the photon energy gets transferred to the electrons in the sample. Two mechanisms play a role here, the photoelectric effect and Compton scattering.

According to the theory of the photoelectric effect, bound electrons can be dissolved from the bond by absorbing a photon that has an energy higher than the binding energy. X-rays always have an energy higher than the typical binding energies of electrons in a glassy material. Hence, this effect would be sufficient enough to ionize molecules in the material.

Compton scattering was already introduced above. An 8 keV photon can transfer a maximum of about 243 eV to an electron. XPS[4] measurements have shown that a electron in the 2p-orbital in a SiO_2 quartz needs an energy of 103 eV[31] to be kicked out of the molecule. The energies must be similar in vitreous silica. Therefore, 243 eV is enough energy to liberate electrons from their molecule via Compton scattering and ionize it.

We have seen now that X-rays provide enough energy for both effects that are causing ionization in molecules. Ionization subsequently causes a change in the complex potential energy landscape of the glass, which could eventually result in a atomic rearrangement. This mechanism could also explain why there is no beam-induced dynamics in metallic samples. Not bounded (conduction) electrons in metals are simply described as a free Fermi gas. In such a gas the electrons are highly delocalized. An absorption of a photon excites the electron in a state of higher energy within the

[3] The cross section is measure for the likeliness that scattering occurs.

[4] XPC is the abbreviation of X-ray photoelectron spectroscopy.

Fermi gas, but does not effect the potential energy landscape of the atomic lattice and no diffusion would occur. Bounded electrons ionized by the photons are, on the contrary, immediately replaced from the pool of conducting electrons and thus the photons impact on atomic bindings in metallic samples is minimized or completely annihilated.

What has not been investigated here is the cross section for the photoelectric effect as well as Compton scattering with electrons. This is mainly because this thesis focuses on the experimental investigation of the effect.

7.3 Outlook

Beam-induced dynamics is understood to some degree now, but there is still more research necessary for full comprehension.

An important question that must be addressed is whether the induced dynamics is temperature-dependent or constant for all temperatures. A possible dependence of the temperature plays an important role in the separation of induced and internal dynamics, as can be seen in Eq. (7.1) and Eq. (7.3) respectively. The dynamics would be easier to separate, if the induced dynamics only adds a constant term to the Arrhenius equation.

At the time this thesis was written, ionization of the atoms seemed to be a suitable candidate for the mechanism behind beam-induced dynamics. However, there is still the possibility that metals also experience beam-induced dynamics, but that they are too fast to be detected by current techniques. Then the reasoning in this thesis regarding the mechanism of ionization cannot hold. If technically possible, aXPCS experiments on a shorter time-scale could answer this question. Free-electron laser seem to be a promising candidate for extending aXPCS to much faster diffusion processes[32].

What is also up for debate is the question of what elements in the material actually move and what the properties of this movements are on the atomic scale. To get an insight into this questions, the correlation time τ as a function of the scattering vector $\mathbf{q}$ could be investigated and then compared to the jump models presented in section 3.4. This would give detailed information on the mean residence time of the atoms, the typical jump lengths and frequencies.

Last but not least, it must be mentioned that beam-induced dynamics is probably different for every material. If this is the case, then the beam-induced diffusion coefficient D_{beam} must be determined for every material that one intends to measure via aXPCS.

Appendix A

Derivation of the optimal sample thickness

The optimal sample thickness W_{opt} is the thickness that maximizes the scattered radiation for a given material and a given scattering angle. The material is characterized by its absorption coefficient μ and the scattering angle 2θ. The absorption coefficient depends on the material used in the experiment. Deriving the optimal sample thickness is a geometrical problem. The situation is shown in Fig. A.1.

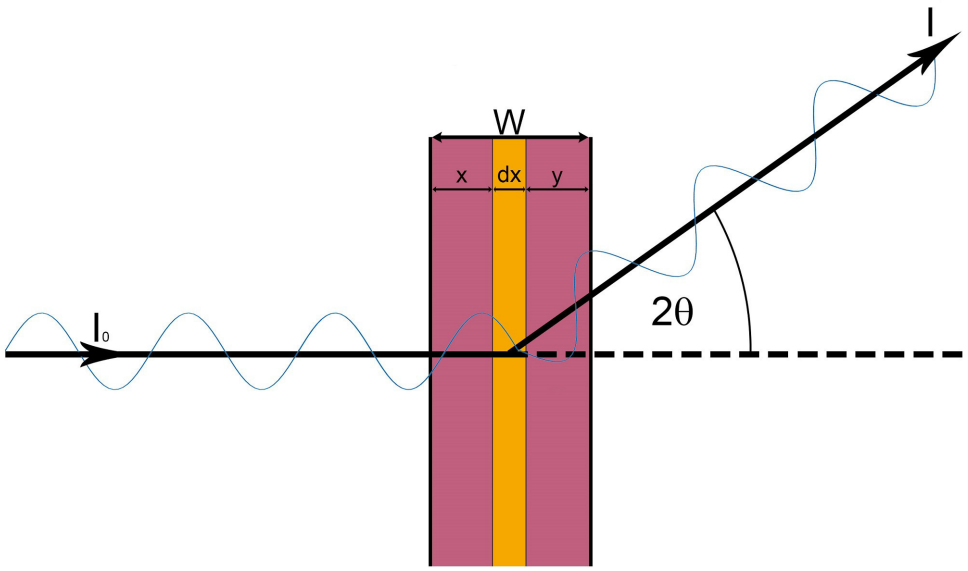

Figure A.1: A synchrotron measurement in transmission geometry.

The part dI of the beam is scattered in an interval dx of the sample. The distance the beam takes in the sample before scattering is x and y after scattering. All measurements in the course of this thesis were conducted in transmission geometry with a beam of intensity I_0 striking the sample perpendicular to the surface. Hence the fraction dI of the beam getting scattered in an infinitesimal interval dx is[8]

$$dI = I_0 e^{-\mu x} s e^{-\mu y} dx \tag{A.1}$$

Integration gives

$$I = I_0 s \int_0^W e^{-\mu(x+y)} dx \tag{A.2}$$

y can be expressed as a function of x, i.e. $y(x) = \frac{W-x}{cos(2\theta)}$, leading to

$$I = I_0 s \int_0^W e^{-\mu(x+\frac{W-x}{cos(2\theta)})} dx =$$

$$I_0 \frac{e^{-\frac{\mu W}{cos(2\theta)}} - e^{-\mu W}}{\mu(1 - \frac{1}{cos(2\theta)})} \tag{A.3}$$

Calculating $\frac{\partial I}{\partial W}$, setting it 0 ans solving the equation for W gives the optimal thickness

$$W_{opt}(\mu, \theta) = \frac{ln(cos(2\theta))}{\mu(1 - \frac{1}{cos(2\theta)})} \tag{A.4}$$

The limit $\theta \to 0$ can be calculated by using L'Hôpital's rule and gives

$$W(\mu, \theta = 0) = \frac{1}{\mu} \tag{A.5}$$

Appendix B

Code for logarithmic binning

```
%%% Import Data %%%
filename = "FILENAME"; %Enter FILENAME here without extension
fullname = [filename ".txt"]; %Filename extension
data = load(fullname);
nrows = rows(data);
%%% Adjust binning factor %%%
binfactor = 1.05;

%%% Logarithmic Binning %%%
jM = zeros(nrows,1);
x1 = 1;
x2 = round(x1*binfactor);

for j=1:nrows
  if(x2<nrows)
    jM(j) = x1;
  else
    break;
  endif
x2 = round(x1*binfactor);
x1 = x2+1;
endfor

counter = 1;
for j =1:nrows
  if(jM(j) != 0)
    counter+=1;
  else
    break;
  endif
endfor

counter -= 1;
```

```
jM2 = zeros(1,counter);

for j=1:counter
  jM2(1,j) = jM(j);
endfor

A = zeros(counter,3);
x1 = 1;
x2 = round(x1*binfactor);
Arow = 1;

for j=jM2
  if (x2 <= nrows)
  for i=x1:x2
    A(Arow,1) = (x1+x2)/2;
    A(Arow,2) = A(Arow,2) + data(i,1);
    A(Arow,3) = A(Arow,3) + data(i,2);
  endfor
  else
  for i=x1:nrows
    A(Arow,1) = (x1+nrows)/2;
    A(Arow,2) = A(Arow,2) + data(i,1);
    A(Arow,3) = A(Arow,3) + data(i,2);
  endfor
  endif

  if (x2 <= nrows)
    A(Arow,2) = A(Arow,2)/(x2+1-x1);
    A(Arow,3) = A(Arow,3)/(x2+1-x1);
  else
    A(Arow,2) = A(Arow,2)/(nrows+1-x1);
    A(Arow,3) = A(Arow,3)/(nrows+1-x1);
  endif

x1 = x2+1;
x2 = round(x1*binfactor);
Arow += 1;
endfor

for i=1:counter
  A(i,1)-=1;
endfor

%%% Saving the data %%%
readoutname = [filename "_logbin.txt"];
dlmwrite(readoutname,A,'delimiter','\t','precision',7)
```

Bibliography

[1] M. Leitner. *Studying atomic dynamics with coherent X-rays*. Springer Science & Business Media, 2012.

[2] B.J. Berne and R. Pecora. *Dynamic light scattering: with applications to chemistry, biology, and physics*. Courier Corporation, 2000.

[3] M. Weik, R. Ravelli, G. Kryger, S. McSweeney, M.L. Raves, M. Harel, P. Gros, I. Silman, J. Kroon, and J.L. Sussman. Specific chemical and structural damage to proteins produced by synchrotron radiation. *Proceedings of the National Academy of Sciences*, 97(2):623–628, 2000.

[4] M. Leitner, M. Stana, M. Ross, and B. Sepiol. Acceleration of atomic dynamics due to localized energy depositions under x-ray irradiation. *arXiv preprint arXiv:1510.01918*, 2015.

[5] B. Ruta, F. Zontone, Y. Chushkin, G. Baldi, G. Pintori, G. Monaco, B. Rufflé, and W. Kob. Hard x-rays as pump and probe of atomic motion in oxide glasses. *Scientific Reports*, 7, 2017.

[6] G. Grübel and F. Zontone. Correlation spectroscopy with coherent x-rays. *Journal of Alloys and Compounds*, 362(1):3–11, 2004.

[7] A. Madsen, A. Fluerasu, and B. Ruta. Structural dynamics of materials probed by x-ray photon correlation spectroscopy. *Synchrotron Light Sources and Free-Electron Lasers: Accelerator Physics, Instrumentation and Science Applications*, pages 1–21, 2014.

[8] M. Ross. *Atomic Diffusion in Glasses Studied with Coherent X-Rays*. Springer Theses. Springer International Publishing, 2016.

[9] C.T. Chudley and R.J. Elliott. Neutron scattering from a liquid on a jump diffusion model. *Proceedings of the Physical Society*, 77(2):353, 1961.

[10] A.J.F. Siegert. *On the fluctuations in signals returned by many independently moving scatterers*. Radiation Laboratory, Massachusetts Institute of Technology, 1943.

[11] D. Lumma, L.B. Lurio, S.G.J. Mochrie, and M. Sutton. Area detector based photon correlation in the regime of short data batches: Data reduction for dynamic x-ray scattering. *Review of Scientific Instruments*, 71(9):3274–3289, 2000.

[12] R. Kohlrausch. Theorie des elektrischen rückstandes in der leidener flasche. *Annalen der Physik*, 167(2):179–214, 1854.

[13] G. Williams and D.C. Watts. Non-symmetrical dielectric relaxation behaviour arising from a simple empirical decay function. *Transactions of the Faraday society*, 66:80–85, 1970.

[14] W. H. Zachariasen. The atomic arrangement in glass. *Journal of the American Chemical Society*, 54(10):3841–3851, 1932.

[15] HAKIM R.M. Electrical conductivity of alkali silicate glasses. *Physics and Chemistry of Glasses*, 12(5):132–138, 1971.

[16] W. Pfeiler. *Statistik, Festkörper, Materialien* -. Walter de Gruyter GmbH & Co KG, M, 2017.

[17] R. Dupree, D. Holland, and D.S. Williams. The structure of binary alkali silicate glasses. *Journal of Non-Crystalline Solids*, 81(1-2):185–200, 1986.

[18] R.K. Brow. the structure of simple phosphate glasses. *Journal of Non-Crystalline Solids*, 263:1–28, 2000.

[19] U. Hoppe, G. Walter, A. Barz, D. Stachel, and A.C. Hannon. The po bond lengths in vitreous probed by neutron diffraction with high real-space resolution. *Journal of Physics: Condensed Matter*, 10(2):261, 1998.

[20] C. Tietz. Investigation of the structure of lithium borate ionic glasses, 2015.

[21] A.H. Verhoef and H.W. Den Hartog. Structure and dynamics of alkali borate glasses: a molecular dynamics study. *Journal of non-crystalline solids*, 182(3):235–247, 1995.

[22] H. Jobic. Diffusion studies using quasi-elastic neutron scattering. *Membrane Science and Technology*, 6:109–137, 2000.

[23] K. Holzweber. Investigating alkali borate glasses via total x-ray scattering, 2017.

[24] W.M. Haynes. *CRC Handbook of Chemistry and Physics, 92nd Edition* -. Taylor & Francis, Justus-Liebig-Universität Gießen, 92. aufl. edition, 2011.

[25] R.D. Greenough, P. Dentschuk, and S.B. Palmer. Thermal expansion of lead silicate glasses. *Journal of Materials Science*, 16(3):599–603, 1981.

[26] D. Ehrt. Structure, properties and applications of borate glasses. *Glass technology*, 41(6):182–185, 2000.

[27] M.G. Strauss, I. Naday, I.S. Sherman, M.R. Kraimer, E.M. Westbrook, and N.J. Zaluzec. Ccd sensors in synchrotron x-ray detectors. *Nuclear Instruments and Methods in Physics Research Section A: Accelerators, Spectrometers, Detectors and Associated Equipment*, 266(1):563–577, 1988.

[28] K.J. McCarthy, A. Owens, and A. Keay. Escape peak ratios in silicon x-ray charge coupled devices (ccds). *Nuclear Instruments and Methods in Physics Research Section A: Accelerators, Spectrometers, Detectors and Associated Equipment*, 384(2-3):403–409, 1997.

[29] N.P. Bansal and R.H. Doremus. *Handbook of glass properties*. Elsevier, 2013.

[30] G.H. Kinchin and R.S. Pease. The displacement of atoms in solids by radiation. *Reports on progress in physics*, 18(1):1, 1955.

[31] R. Nordberg, H. Brecht, R.G. Albridge, A. Fahlman, and J.R. Van Wazer. Binding energy of the" 2p" electrons of silicon in various compounds. *Inorganic Chemistry*, 9(11):2469–2474, 1970.

[32] F. Lehmkühler, P. Kwaśniewski, W. Roseker, B. Fischer, M. A. Schroer, K. Tono, T. Katayama, M. Sprung, M. Sikorski, S. Song, et al. Sequential single shot x-ray photon correlation spectroscopy at the sacla free electron laser. *Scientific reports*, 5:17193, 2015.

Acknowledgements

Finally I would like to acknowledge all my colleagues and co-workers from in- and outside the university. Without them this thesis would not have been possible.

I would first like to thank my thesis advisor Prof. Bogdan Sepiol for giving me the opportunity to work in his research group and take part in their scientific journey. I am also grateful for his continuous support and expertise throughout all time of research and writing. Beside my advisor, I would like to thank my colleagues Katharina Holzweber and Christoph Tietz for their assistance in any regard, the stimulating discussions and all the fun we had in the last year.

I'd like to give special thanks to my parents for their support and encouragement, without whom I would never have enjoyed so many opportunities.

Last but not least, I thank our group head Prof. Herwig Peterlik, our administrative assistant Yvonne Simon and all others who were involved in the process, but not mentioned here for making this possible.